2020

Southern Ocean Aerosol Optical Depth - instrument comparison and Maine Aerosol Network Validation

Samantha Orum

Southern Ocean Aerosol Optical Depth - instrument comparison and Maine Aerosol Network Validation

Abstract

A series of atmospheric instruments were deployed aboard the research vessel RV *Investigator* for a 42-day campaign in 2018 to quantify aerosol optical depth and the properties associated with aerosol in the Southern Ocean marine boundary layer between Australia and Antarctica. The optical depth measurements collected via Microtops sun photometers and LiDAR were analysed for data compatibility to increase the dataset. It was found that aerosol optical depth that was derived from the day-time LiDAR measurements were too noisy to be compatible with the known optical depth measurements. However, an analysis exploring optical depth measurements derived from night-time data indicated moderate compatibility with the known measurements and could be analysed in future studies. Three cases studies, two high aerosol optical depth periods (means of 0.22 and 0.198) and one low period (mean of 0.061), were identified for analyses from the data collected by the Microtops II sun photometer. Data reviewed from LiDAR including cloud type and attenuated backscatter alongside backward trajectory wind path models showed physical mechanisms that were consistent with sea spray aerosol production for the two high periods. The third period which experienced low optical depth and was the closest period to Antarctica indicated sea ice and continental influence, reducing the aerosol formation

Degree Type

Thesis

Degree Name

Bachelor of Environmental Science (Honours)

Department

School of Earth, Atmospheric and Life Sciences

Advisor(s)

Stephen Wilson

Keywords

aerosol optical depth, lidar, sunphotometer

Southern Ocean Aerosol Optical Depth - instrument comparison and Maine Aerosol Network Validation

Samantha Orum

20 October 2020

A thesis submitted in part fulfilment of the requirements of the Bachelor of Environmental Science (Honours) in the School of Earth, Atmospheric and Life Sciences, Faculty of Science, Medicine and Health, University of Wollongong 2020.

October 2020

Certification

I, Samantha Orum, declare that the information in this thesis is entirely the result of investigations conducted by myself, unless otherwise acknowledged, and has not been submitted in part, or otherwise, for any other degree or qualification.

Samantha Orum

Abstract

A series of atmospheric instruments were deployed aboard the research vessel RV *Investigator* for a 42-day campaign in 2018 to quantify aerosol optical depth and the properties associated with aerosol in the Southern Ocean marine boundary layer between Australia and Antarctica. The optical depth measurements collected via Microtops sun photometers and LiDAR were analysed for data compatibility to increase the dataset. It was found that aerosol optical depth that was derived from the day-time LiDAR measurements were too noisy to be compatible with the known optical depth measurements. However, an analysis exploring optical depth measurements derived from night-time data indicated moderate compatibility with the known measurements and could be analysed in future studies. Three cases studies, two high aerosol optical depth periods (means of 0.22 and 0.198) and one low period (mean of 0.061), were identified for analyses from the data collected by the Microtops II sun photometer. Data reviewed from LiDAR including cloud type and attenuated backscatter alongside backward trajectory wind path models showed physical mechanisms that were consistent with sea spray aerosol production for the two high periods. The third period which experienced low optical depth and was the closest period to Antarctica indicated sea ice and continental influence, reducing the aerosol formation.

Contents

List of Figures

List of Tables

Acknowledgements

Firstly, I would like to thank my supervisors, Stephen Wilson and Ruhi Humphries, both of whom guided me through this thesis with so much humour and patience. You each taught me so much about a atmospheric science, a field I knew very little about 10 months ago. Stephen, thank you for being you giving with your time. You allowed me to feel comfortable asking you even the silliest of questions. Ruhi, thank you for sharing so much of your journey from your Honours years through to Chief Scientist! Our conversations inspired me when making my own decisions for my career and I am immensely grateful. Each of you made this project and the science surrounding it so exciting and engaging even through such a difficult period, I can't think of any two greater people to have completed this project with. Thank you, thank you, thank you.

Thank you Simon Alexander, for being so willing to teach me about lidar and providing the backscatter and cloud type graphs used within this report. Our meetings with you were some of my favourite this year.

Serena Cortijo, there are no words to describe my gratitude. After everything we've been through this year, I'm so grateful that you were the one that I got to experience it all with.

Thank you to Courtney Hildebrandt. Your constant encouragement, availability to proof read this report and perhaps, most importantly, your ability to teach almost any software to all of your peers has saved this project and may others. I am so excited to see the incredible things you pursue within your career and life.

To my peers and friends in the Honours room, thank you for being my sound board and my motivation.

To Sapphire and Tom, thank you for giving me the year to complain, to lock myself away to write for hours on end and to speak about nothing but this project for 80% of our conversations. You gave me the home and support I needed during a time that was difficult for all of us, but I am so happy to have been stuck at home with you.

To my family, Mum and Dad, James and Chloe, Aunty Lara and Uncle Barry, and Miss Sharon, I love you all so much.

James and Chloe, thanks for keeping me humble and never letting me take myself too seriously, one day I hope to be as cool as the two of you. Aunty Lara and Uncle Barry, thank you for allowing you home to be my haven too and your constant support and love. Beautiful Miss Sharon, thank you for keeping me sane with your words of encouragement of whenever this year got hard.

Dad and Mum, if I used up all my luck getting you two, I will still be set for life. Dad, thank you for inspiring my love for the environment. Listening to your stories of your adventure's world, watching you care about the environment and create a jungle at wherever we go is what made me want to explore and understand the world. You enabled

so many incredible experiences within my career and raised all of your children with the bravery to face any challenge. Mum, thank you for being my confidant, my rock, for pushing me to go to university and for your unconditional pride and support in everything I want to do. Everything I have achieved is due to the both of you.

Abbreviations

Table 1: Abbreviations used within this report

Abbreviation	Expanded Term
AERONET	Aerosol Robotic Network
AOD	Aerosol Optical Depth
BAPS	Baseline Air Pollution Station
CAPRICORN	Cloud, Aerosols, Precipitation, Radiation, and Atmospheric Composition over the Southern Ocean
IR	Infra-Red Waves
LW	Liquid Water
MAN	Maritime Aerosol Network
MBL	Marine Boundary Layer
NASA	National Aeronautics and Space Administration
SLW	Supercooled Liquid Water
UV	Ultra-Violet Waves

Part I

1 Introduction

1.1 The Earths Climatic Systems

The Earths climate is not only reliant on the atmospheric system, but on physical, chemical and biological processes within other components of the Earths system Wallace and Hobbs (2006). The Earth's climate arises from the interaction of five major climatic systems: the atmosphere, the lithosphere, the hydrosphere, the cryosphere and the biosphere. The feedback processes between these systems are influenced by external factors, both of natural and anthropogenic origin as shown in Figure 1. The anthropogenic activities have caused significant impact on each of the five systems. As the atmosphere is considered the most erratic and changing system, it is imperative to understand the climate and the factors that affects its variations in order to possibly predict the changes of the climate brought by anthropogenic activities (IPCC, 2013).

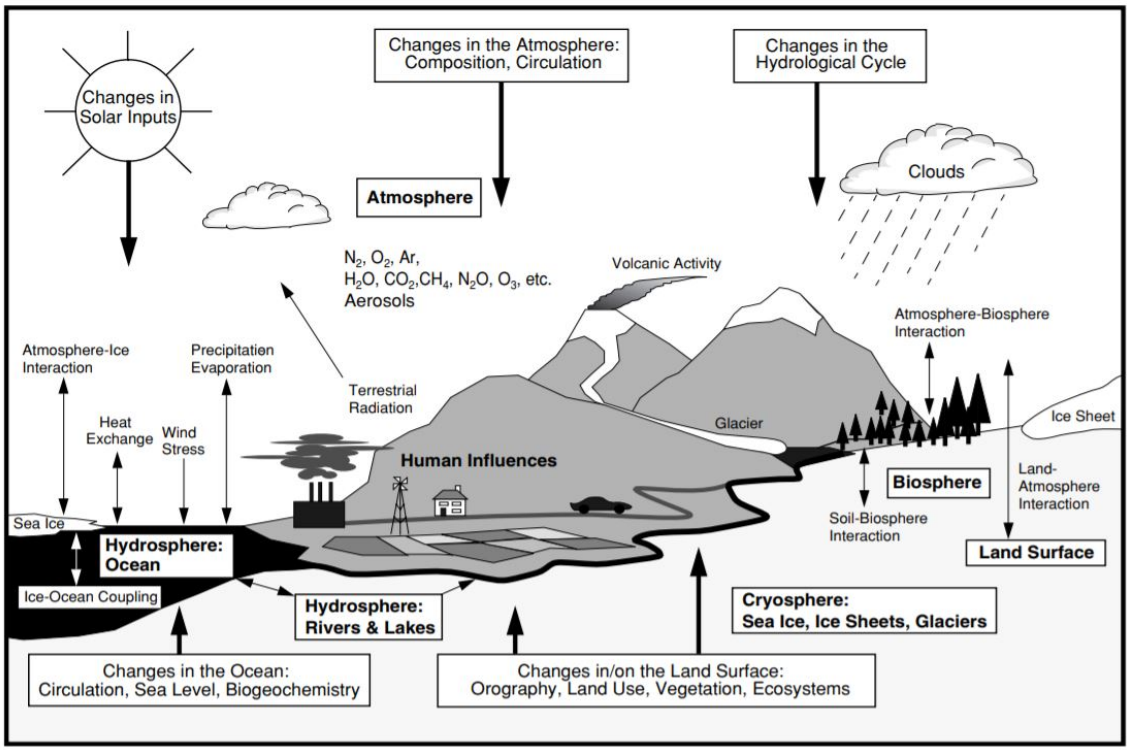

Figure 1: Global climate system components (bold) with their processes and interactions (thin arrows consistent interactions, bold arrows changing interactions) (IPCC, 2013).

The climate is defined as composite of the prevailing weather conditions of a region over a number of years, including: the average temperature, precipitation, air pressure, cloudiness, wind speed and direction and humidity (IPCC, 2013). The climate is driven

as a whole on factors that influence the radiative balance such as solar radiation, the atmospheric composition and volcanic eruptions. The Sun's radiation is a driving source of energy for the lower atmosphere known as the troposphere (IPCC, 2013). The Earth receives an average of 342 W.m^{-2} per year across its spherical surface of the atmosphere and a significant portion (31%) is immediately reflected back into space by clouds and the Earth's surface. The remaining 235 W.m^{-2} is absorbed by the atmosphere and remaining climate systems, warming the Earth's land and oceans (IPCC, 2013). The Earth's surface also releases stored heat (thermals) to the atmosphere (Figure 2). The exchange of heat energy between the surface and atmosphere of the Earth maintains the global mean temperature at 14°C at the surface, which decreases with increasing altitude to reach a mean temperature of -58°C a the top of the atmosphere. These heat exchanges are shown in Figure 2. The Sun radiation, some of which are between Infra-Red (IR) and Ultra-Violet (UV) wavelengths, are effectively absorbed by greenhouse gases in the atmosphere, resulting in its warming. The short-term imbalance of net incoming and outgoing radiation in the atmosphere is primary caused by the composition of the atmosphere, after which the climate system re-establishes equilibrium after several years.

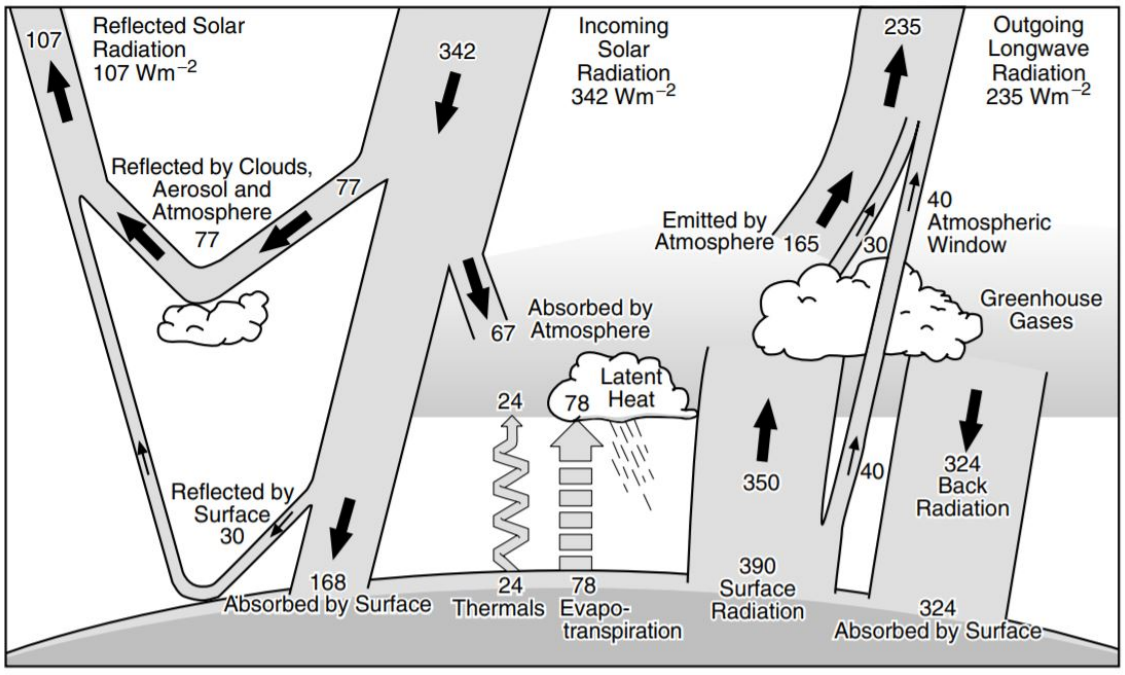

Figure 2: The Earth's annual and global mean energy balance. Of the incoming solar radiation, 49% (168 Wm^{-2}) is absorbed by the surface. That heat is returned to the atmosphere as sensible heat, as evapotranspiration (latent heat) and as thermal infrared radiation. Most of this radiation is absorbed by the atmosphere, which in turn emits radiation both up and down. The radiation lost to space comes from cloud tops and atmospheric regions much colder than the surface. This causes a greenhouse effect (IPCC, 2013).

The atmosphere is considered the most variable of the system as it is constantly changing (IPCC, 2013). Climate is determined by the atmospheric circulation and its interactions with the large-scale ocean currents and lands features such as albedo, soil

moisture and vegetation. The composition of the system has changed alongside the evolution of the Earth. Water vapour (H_2O), which is highly variable in the atmosphere, is typically found in the order of 1% at ground level. Excluding water vapour, the dry atmosphere consists of mainly nitrogen (N_2, 78.1%), oxygen (O_2,20.9%) and argon (Ar, 0.93%). Each of these gases have limited interaction interaction with incoming solar radiation and no interaction with infrared wavelengths emitted by the Earth. However, greenhouse gases (trace gases such as carbon dioxide CO_2, methane CH_4, nitrous oxide N_2O, and ozone O_3) encompass less than 0.1% of the dry air. These greenhouse gases exist within the ozone layer, and are particularly susceptible to absorbing and trapping incoming solar radiation causing warming.

1.1.1 The structure of the atmosphere

The atmosphere is a complex and integral part of the Earth's system, which includes internal and external forcing mechanisms which act upon the Earth itself. The atmosphere consists of layers of gases surrounding the Earth as depicted in Figure 3. Each layer can differ in height around different regions of the world and are instead characterised by physical features such as temperature (Goody, 1995). There are 4 major layers; the thermosphere, the mesosphere, the stratosphere and the troposphere. The top most layer is the thermosphere and experiences temperature that is directly proportional to altitude. This is because this is the first layer that interacts with the Sun's radiation, thus absorbing and scattering a significant portion of its heat (Wallace and Hobbs, 2006). Below that is the mesosphere, through which the temperature begins to increase with decreased altitude. It also has very low pressure caused by the lack of air above it (Wallace and Hobbs, 2006). The next layer is the stratosphere which houses the ozone layer. The ozone layer, which holds most of the greenhouse gases, warms the layer due to the high absorption and scattering of UV rays (Wallace and Hobbs, 2006). Finally, the troposphere can reach altitudes of eight to eighteen km above the Earth (Figure 3). From the Earth's surface, the temperature decreases with increased altitude. The boundary between the troposphere and the stratosphere is defined as the temperature increases again. The boundary between the layers is called the tropopause and marks the highest point at which weather can occur (Wallace and Hobbs, 2006).

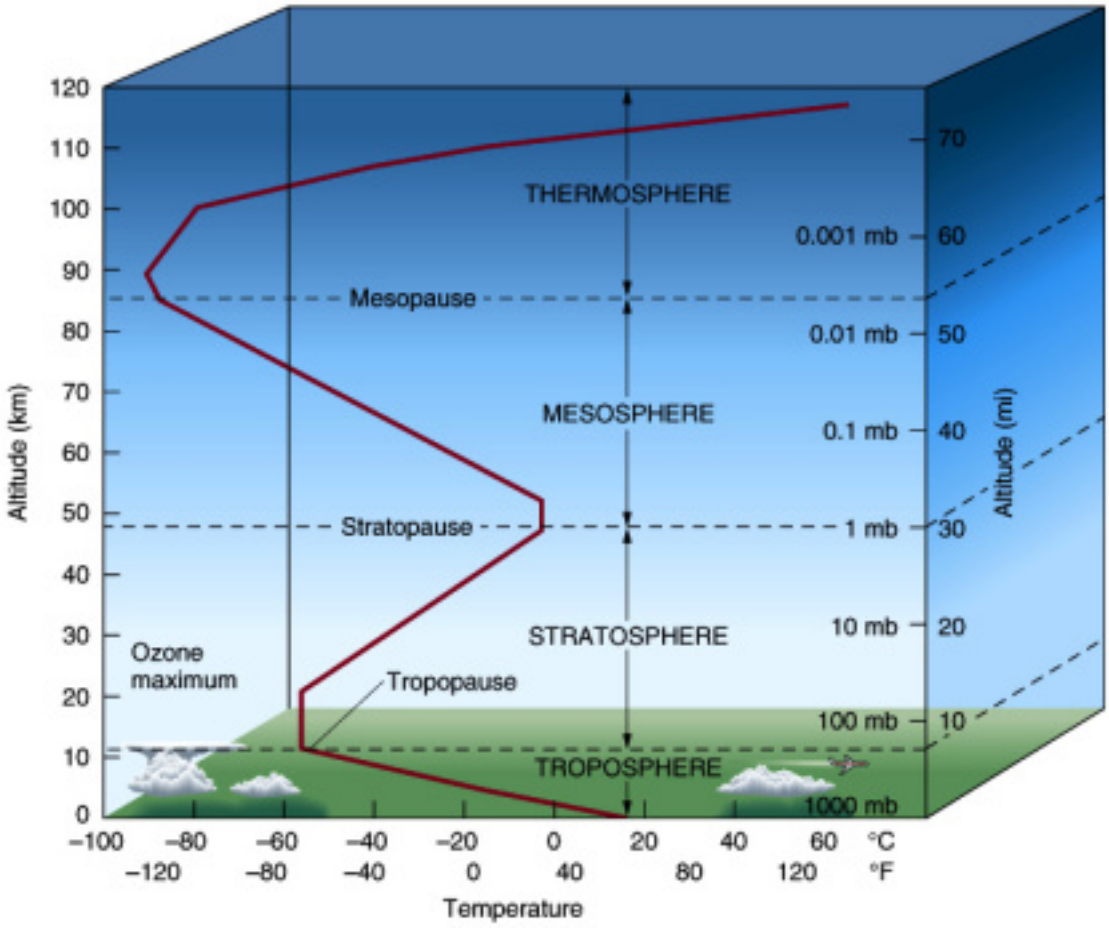

Figure 3: The vertical structure of the atmosphere and the latitudes of each layer. The average temperature and pressure of each layer is also scaled (Chimot, 2017).

At the surface there are two more layers. These are called the planetary boundary layer and the marine boundary layer (MBL) and are located within the troposphere. As the marine and planetary boundary layers interact with the Earth's surface they are directly influenced by the physical, biological and chemical processes (Goody, 1995; Sikora and Ufermann, 2004). The MBL is where the ocean and the atmosphere interact, exchanging large amounts of heat, moisture and momentum (Sikora and Ufermann, 2004).

The movement of global atmospheric circulation occurs in a very specific pattern that is driven by the Earths rotation and the differential solar heating of its surface. The atmospheric circulation can be described as a three cell model as shown in Figure 4 (Wallace and Hobbs, 2006; Lumen, 2020). The first is the Hadley cell, which is located at the equator. The equator is the region that is most intensely heated by the Sun, causing air to rise and create a low-pressure zone. Whist the air rises, it cools and forms thick storm (cumulonimbus) clouds. As it continues to rise, several mechanisms occur. Firstly, the air separates and moves both north and south of the equator. When it reaches approximately 30° north and south, the air cools and sinks towards the surface, forming the subtropical high-pressure zone (Wallace and Hobbs, 2006; Lumen, 2020).

Secondly, as the sir sinks, it warms and dries as the temperature increases. This creates desert areas of little cloud and low rainfall, such as the deserts found in northern Africa (Figure 4).

In the Northern Hemisphere, the northeasterly trade winds flow to the right, and southeasterly trade winds flow to the left in the Southern Hemisphere. This is caused by Coriolis forcing and friction. Coriolis force effect is the apparent force caused by the rotation of the Earth which deflects the movements of objects that are not connected to the ground, such as particles and wind (Wallace and Hobbs, 2006). The effect is caused by the significant difference in speed of the Earths rotation at its equator (1600 km/hr) and the poles (0.00008 km/hr) (Wallace and Hobbs, 2006). If a plane were to immediately fly from Darwin down to Adelaide, Australia in a straight line, it would appear to deflect to the left of the city as it is moving slower has not caught up yet. This deflection to the left occurs everywhere in the Southern Hemisphere, causing air currents to travel to the left. In the Northern Hemisphere, the Coriolis effect behaves in the opposite way, causing the currents to deflect to the right. The direction of movement of wind is detailed on Figure 4 by the white arrows.

The Ferrel cell occurs between latitudes 30° - 60° north and south of the equator. The air on the surface is pulled toward the poles, forming south westerlies in the northern hemisphere, and north westerlies in the southern hemisphere. These tropic winds are warm and collect moisture as they travel over the oceans. At 60° north and south, the tropical winds meet dense, cold air that has drifted from the poles. Due to the difference in density between the warm and cool air an uplift is formed where the two air masses meet. This causes low pressure called the subpolar low at the surface and unstable, wet and windy weather (Wallace and Hobbs, 2006).

The final cell is the Polar cell. At the poles the air is cooled and sinks towards the ground, forming high pressure known as the polar high. The air then drifts toward the lower altitudes before reach the warm topical air brought by the Ferrel cell at 60° north and south. The boundary between the warm and cold air is called the polar front (Lumen, 2020).

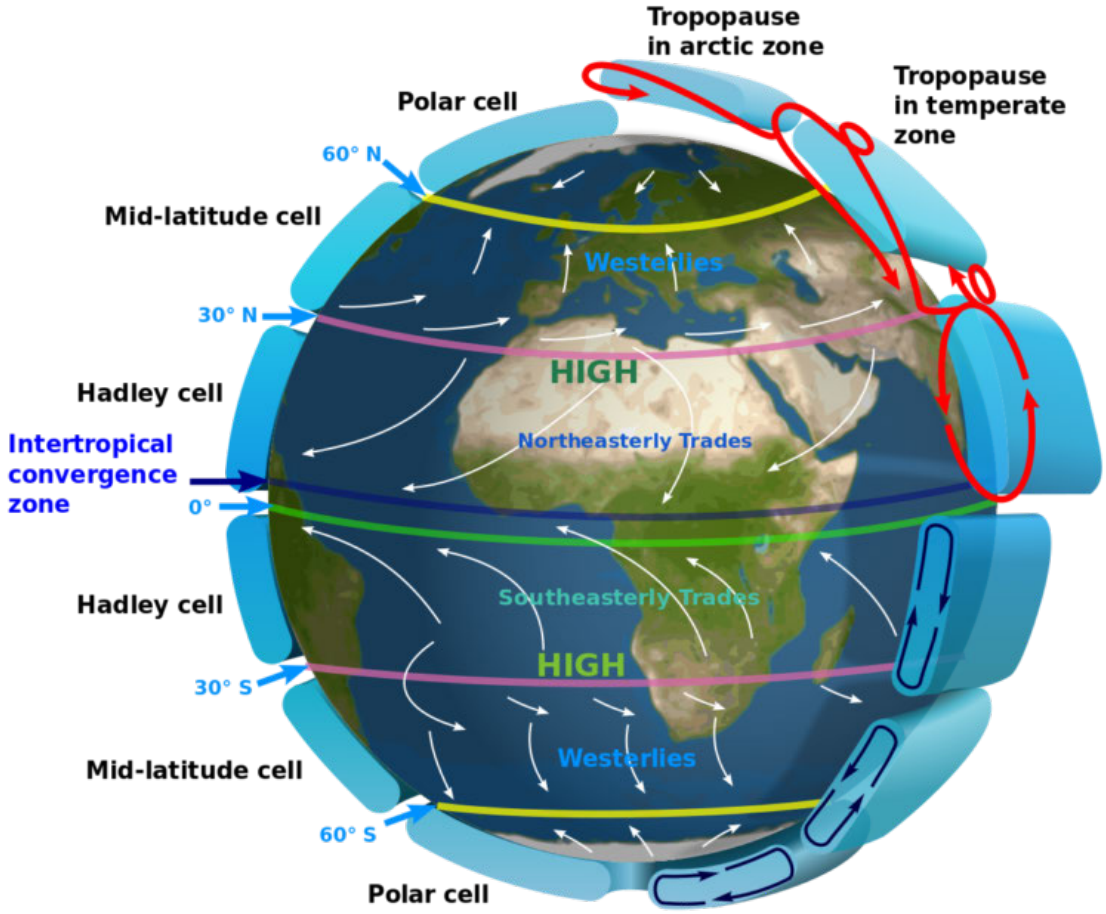

Figure 4: The three-cell model of global atmospheric circulation (Lumen, 2020).

1.2 Aerosols

To understand the chemical composition of the atmosphere, it is fundamental to understand the physical and optical properties of aerosols (Wilson & Forgan, 2001). Aerosol is a suspension of non-gaseous particulates within a gaseous matrix. An atmospheric aerosol is a population of liquid or solid particle that is suspended within the troposphere and stratosphere and can significantly affect local and regional climates by absorbing and scattering incoming solar radiation (Alexander and Protat, 2019). Due to the appreciable influence aerosols have over climate and atmospheric processes, it is important to understand rates of the occurrence, residence time, physical properties, chemical composition and corresponding complex-refractive-index characteristics of the particles.

1.2.1 Aerosol formation

Aerosols can be emitted into the atmosphere naturally or anthropogenically via a wide range of physical mechanism allowing for particles to be released directly into the atmosphere (primary) or chemical reactions which form aerosols through gas to particle conversion

processes (secondary). Oceans around the world produce a significant portion primary and secondary natural aerosols that impact the earths climate. However, as aerosols can be formed by numerous mechanism, understanding the physical parameters that cause its production assists in understanding why there is an increase or decrease in the number of particles in a region.

For example, a sea-spray is major contributor aerosols in the MBL. However, for sea-spray be produced, waves need to be of the breaking variety. Therefore, there are three physical parameters that can be used to determine if sea-spray aerosols are being produced which are: wind speed, sea ice cover, and surface water temperature (Merkulova *et al.*, 2018). Wind stresses the oceans surface and as wave break, air becomes entrained within the water. This causes air bubbles to rise to the surface and the waves to become whitecapped (white coloured). When the air bubbles burst, aerosol droplets are released into the MBL. The effect of increasing wind speed is highly non-linear and results in approximately a factor of ten increase in sea-spray emission per increase of 10 m/s (Merkulova *et al.*, 2018). Secondly, the change in water temperature affects the bubble spectra by influencing the surface tension, viscosity, oxygen saturation and other physiochemical characteristics. It is generally found with increased water temperature, there is a decrease in aerosol production (Merkulova *et al.*, 2018). Finally, sea ice covers the oceans surface, acting as a barrier to the wind and wave breakage which is required for the aerosol formation.

Other common types of primary atmospheric aerosols include mineral or volcanic dust, smoke, soot or organics. Some secondary atmospheric aerosols are sulphates, such as dimethyl sulphides (DMS), nitrates and some organics. Both anthropogenic and naturally occurring aerosols can cause significant effect on local and regional climates, although natural sourced aerosols still predominate at a global scale.

1.3 Aerosol optical depth (AOD)

Aerosol optical depth is a dimensionless measurement of the extinction of direct sunlight by particles in the atmosphere. Particles block sunlight by absorbing or scattering light, thus reducing visibility. AOD value details the amount of aerosol in the vertical column of atmosphere over the observational location. For example, an AOD of less then 0.1 is described as 'clean' and the sky would appear clear and blue, with a bright sun and maximum visibility to the observer. A sky with AOD of 0.4 would appear hazy in comparison .

AOD can be measured by several different types of instruments either directly or indirectly. Within this thesis, the two instruments that care compared are the hand-held Microtops II sun photometer (referred to as 'Microtops sun photometer') and light detection and ranging (LiDAR) instruments.

1.3.1 Sun photometer instruments

A sun photometer is an electronic device that measures direct sunlight over a narrow range of wavelengths. It is used to calculate AOD through the basic operating principle that directed sunlight is scattered and absorbed by the atmosphere it passes through; it is then the amount of light that is diminished at the Earth's surface that shows the amount of aerosols is in the atmosphere (Brooks, 2008). Sun photometers can measure AOD over five wavelengths as well as water vapour and Angstroms exponent for the wavelengths. Sun photometers are considered the most accurate instrument for detecting AOD but have the additional complexity that the sensor must be directly pointed at the sun (within 1°-3° field of view) without any cloud obstruction (Porter *et al.*, 2010).

1.3.2 Principles of LiDAR aerosol and AOD measurements.

LiDAR instruments are essential in understanding and profiling the atmosphere (Wandinger, 2005; Alexander and Protat, 2019). Since the early 1960's, cloud and aerosol layers have been investigated using elastic-backscatter LiDAR (i.e. Rayleigh), however only since the early 2000's has there been significant quantitative studies of atmospheric aerosol properties based on LiDAR (Ansmann and Muller, 2005). This is largely due to LiDAR being able to provide the unique capability profiling the vertical structure of aerosol backscatter by identifying the aerosol scattering as a function of the altitude (Alexander and Protat, 2019).

LiDAR can be used to measure a variety of atmospheric properties including cross-polarisation backscatter, co-polarisation backscatter and depolarisation which can be used to classify cloud types and aerosol in within the vertical structure (Alexander and Protat, 2018, 2019). The aerosol extinction is dependent on the absorption and scattering of the lasers light, the LiDAR ratio can be used to measure the absorption of aerosol particles (Alexander and Protat, 2019). As backscatter and aerosol extinction are wavelength dependent, the development of the multi-wavelength Raman LiDAR systems have enabled the characterisation of both LiDAR ratios and Angstroms exponents (Alexander and Protat, 2019).

1.4 Established Baseline Air Pollution Stations within the study area

Established measurement sites for cloud and aerosol properties within the area of study for this thesis are important to understanding normal and abnormal events that are present within the data. The Cape Grim Science Program was created from a commitment by the Australian Government to the United Nations Environment Program in the early 1970's to monitor and study global atmospheric composition for climate change as a resulted of human activities and natural variability (Crawford *et al.*, 2017). This resulted in the establishment of the Cape Grim Baseline Air Pollution Station (BAPS) in April

1976, to measure the composition of the atmosphere and has been operating continuously ever since (Ayers *et al.*, 1997; Crawford *et al.*, 2017). Located on the north-west tip of Tasmania, Cape Grim BAPS is one of 3 Premier Global Baseline Stations around the world and is able to measure 'true background air' (Ayers *et al.*, 1997). This is air that is uncontaminated by point sources when the wind blows in from the south-west across the Southern Ocean as depicted in Figure 5. The management of Cape Grim's BAPS is a joint responsibility of the Australian Bureau of Meteorology (BoM), which funds and operates Cape Grim's BAPS, and the Commonwealth Scientific and Industrial Research Organisation (CSIRO) who manages the science program. The collaborators of the science program include the University of Wollongong and the Australian Nuclear Science and Technology Organisation alongside other institutions, in order to analyse and model the resultant data collected at the site (CSIRO, 2020a). Over 40 years of the consistent data collection has enabled for a substantial body of observational research of aerosol and aerosol-related measurements (Ayers *et al.*, 1997). Cape Grim is a key reference site for comparison within this thesis due its proximity and significant body of historical data.

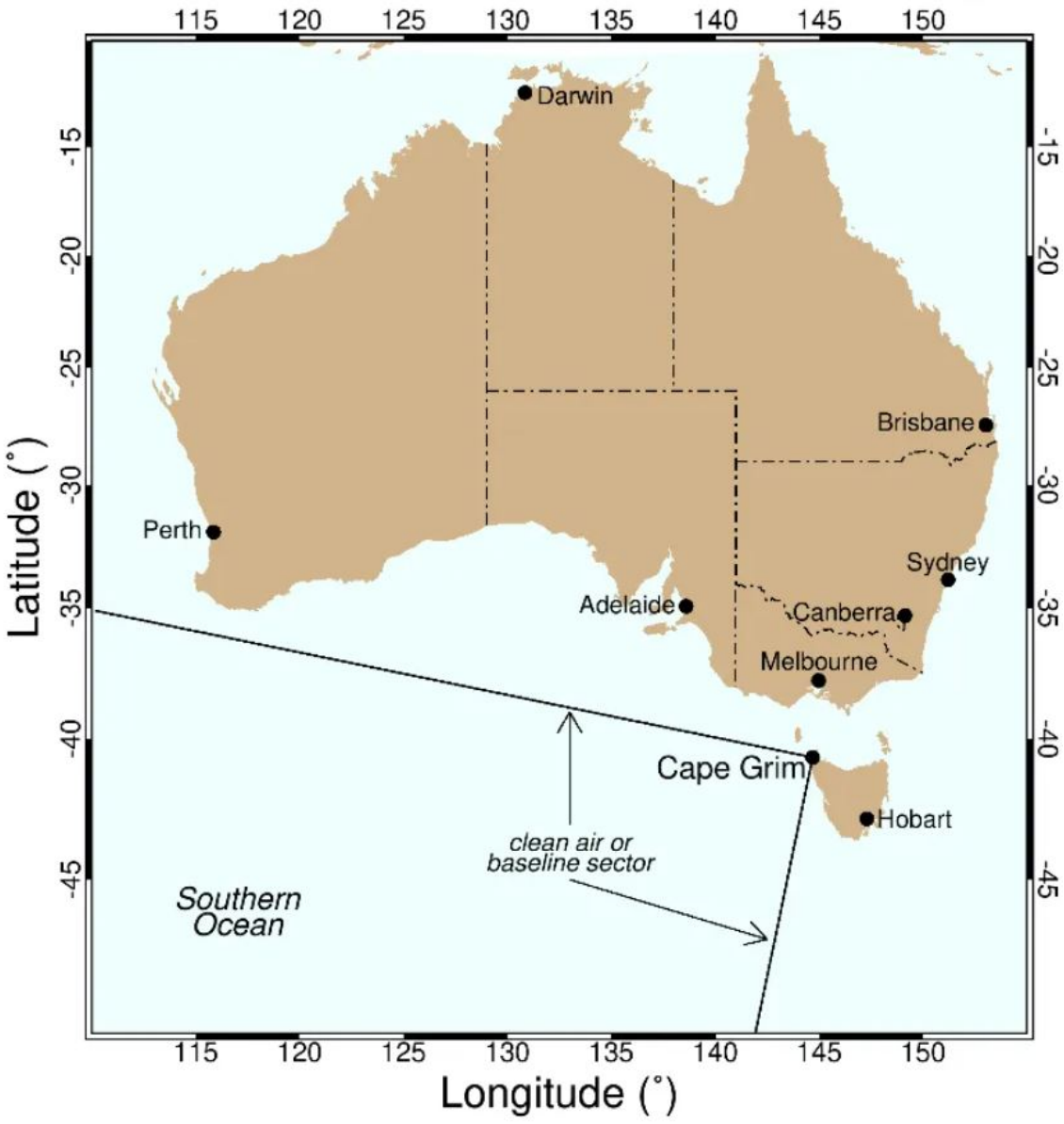

Figure 5: Cape Grim is positioned on the isolated north-west tip of Tasmania and receives true baseline air from the south-west, over the Southern Ocean CSIRO (2020a).

1.5 Maritime Aerosol Network

The Maritime Aerosol Network (MAN) was developed as a component of the Aerosol Robotic Network (AERONET) with the aim to address the need to improve atmospheric aerosols models with up-to-date data that is collected over the worlds oceans (Smirnov *et al.*, 2009). MAN was evolved around the opportunity to use handheld sun photometer measurements on various scientific and non-scientific ships; a data set that could compliment the vast island-based AERONET measurements (Smirnov *et al.*, 2009). The principle scientific objectives of MAN are studies of climate change, satellite retrieval validation, verification of global aerosol transport models, existing gaps in global aerosol distribution and validating the representativeness of island measurements (Smirnov *et al.*, 2009).

MAN employs a measurement protocol that is described in the operational methods (2.1.3) of this thesis. The measurement points are grouped temporally into series; if the interval between 2 points is greater then 2 minutes, they are placed within different series. MAN then assures the data quality through a filtering system. First, the Level 1.0 (unscreened) measurement series are used to plotted with a cloud and pointing error screening applied. MAN's screening follows the criteria for cloud and pointing errors as follows:

1. *Within a series, the minimum AOD for each point is identified at each wavelength* (τ_{ai}^{min})

2. *If the difference* ($\tau_{ai} - \tau_{ai}^{min}$) *for each spectral channel is less than the maximum of* $\{\tau_{ai}^{min} \times 0.05, 0.2\}$*, the the point within a series is considered cloud-free and pointing is error free. If the above screening removes all but one point from a series, then an following additional criterion is applied to the spectral channels;*

   (a) *If the Angstroms parameter computed using all available channels between* 440 *and* 870 *nm is greater than* -0.1*, then the point is considered cloud and pointing error free.*

Once the series is screened, it becomes the Level 1.5 data set. Finally, Level 1.5 data sets undergo a final calibration of the values, spectral channels are evaluated for filter degradation and other instrumental errors or data anomalies and manual data inspection is completed for possible outliers. The data is then classed as Level 2.0 is quality-assured by MAN.

Since late 2006, regular measurements in various oceanic regions have been collected in association with MAN; all of the data can be found at on the MAN website and is accessible to the public.

1.6 CAPRICORN Campaigns

There have been two research voyages upon the Australian ship Research Vessel *Investigator* (RV *Investigator*) for the Cloud, Aerosols, Precipitation, Radiation, and Atmospheric Composition over the Southern Ocean (CAPRICORN) south of Australia (Mace and Protat, 2018). The objectives of CAPRICORN, as described by Mace and Protat (2018), were as follows:

- to characterise the cloud, aerosol and precipitation properties, boundary layer structure, biological production and cycling of DMS in the upper ocean, atmospheric composition, boundary layer structure, and surface energy budget alongside their latitudinal variability;

- evaluate and improve satellite estimations of the listed properties

- evaluate and improve the representation of the listed properties in the regional and global versions of the Australian Community Climate and Earth-System Simulator.

The first voyage went for 5 weeks, beginning on the March 13th, 2016 and concluding on April 15th, 2016. The campaign departed from Hobart and covered the latitudes between 43°S and 53°S. A second, more extensive voyage was conducted in 2018 and is the focus of this thesis.

1.7 Overall Aim and Description of Study

The purpose of this thesis was to investigate the aerosol optical depth measurements that were collected during the 2018 CAPRICORN II campaign and to compare various instruments that could be used to measure optical depth. An analysis will be conducted in the following chapters within which the data processing techniques will be critiqued and two AOD measuring instruments will be compared. Finally, a case study in which three periods of high and low AOD measurements during the campaign will be analysed to determine possible causes of increased aerosols.

Part II

2 Methods

2.1 Operational Methods

2.1.1 RV *Investigator* Measurement Platform

The RV *Investigator* is a 94-metre long blue-water research vessel managed and operated by Marine National Facility on behalf of the Australian Government. Propelled by a diesel-electric motor, the vessel is capable of delivering up to 300 research days per year. Commissioned and built in 2014, the vessel was purposely built to possess a wide range of on-board and modular laboratories and facilities (CSIRO, 2020b). Additionally, the ship was designed with flexible platform capabilities to support multi-disciplinary scientific research in biological, oceanographic, geological and atmospheric fields alongside maritime training and education (CSIRO, 2020b). The large range of onboard equipment that is exclusively used for atmospheric research includes a weather radar, instruments that measure sunlight, aerosols microphysical and optical properties, as well as reactive gases and greenhouse gases (CSIRO, 2020b).

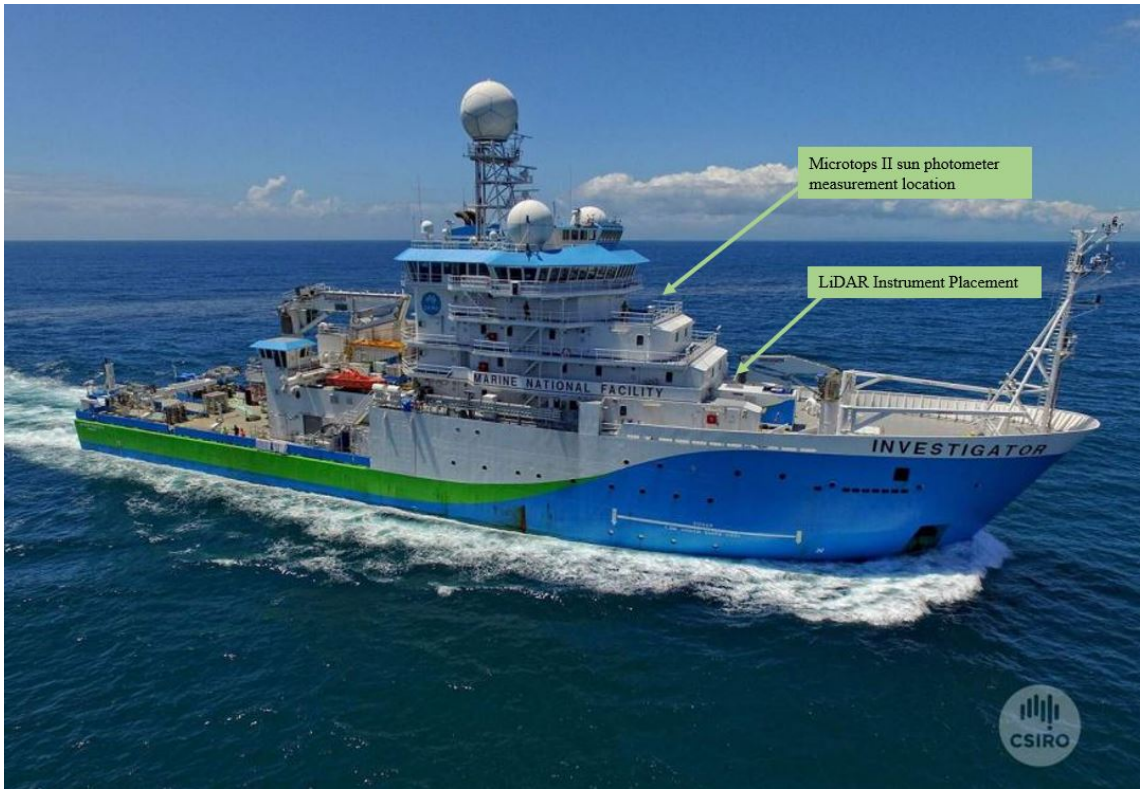

Figure 6: The RV *Investigator* with the sampling location the Microtops II sun photometer was used and the LiDAR instrument placement during the CAPRICORN II campaign (CSIRO, 2020b).

2.1.2 CAPRICORN II Voyage Summary

The CAPRICORN II voyage was conducted during the summer of 2018 aboard the RV *Investigator*. The research vessel departed from Hobart, Australia on the January 11th and returned on the February 22nd, 2018, after a total of 42 days at sea. During the voyage period, the RV *Investigator* reached 66°S (Figure 7) and the trip was conducted entirely within the open water of the Southern Ocean. There was an extensive suite of atmospheric remote-sensing instruments aboard the vessel during the voyage, as the purpose of the trip was to gain a thorough understanding of the atmospheric conditions and composition.

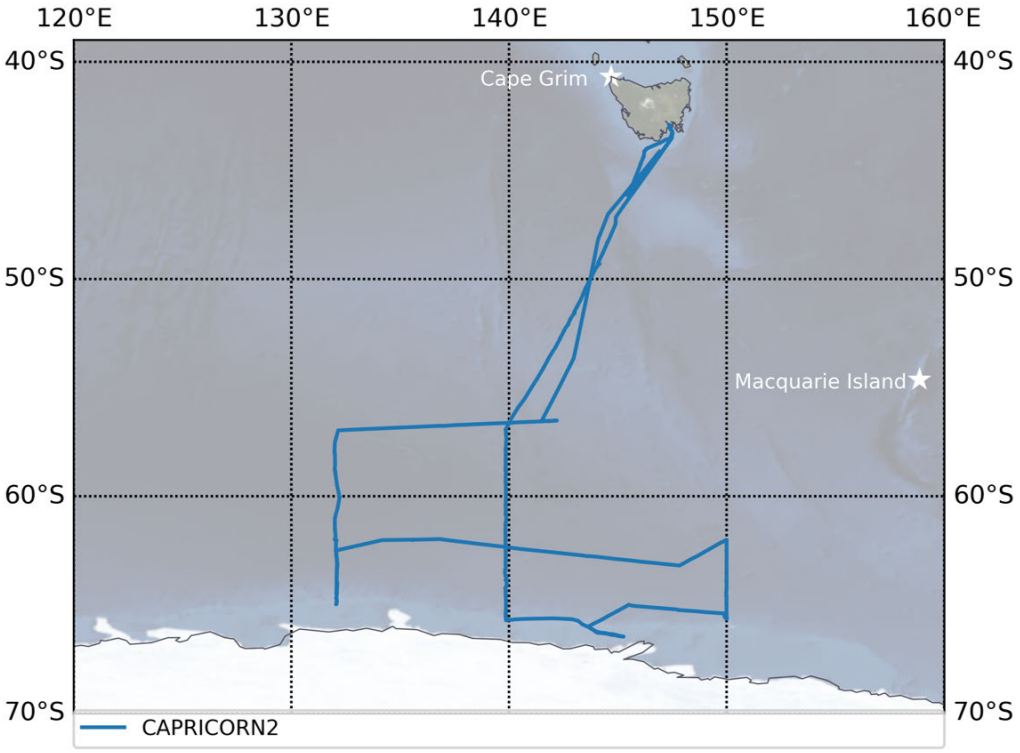

Figure 7: Voyage track of the RV *Investigator* for the CAPRICORN II (13 January to 19 February, 2018, blue). The ship's position is shown at midday (UTC) for the days in which Microtops sun photometer AOD measurements were collected. Nearby Baseline Air Pollution Stations at Cape Grim and Macquarie Island have also been identified with a star (R. Humphries, 2020).

2.1.3 Hand-held Microtops II sun photometer

The sun photometer instruments that used during the campaign was the Microtops II sun photometer (referred to as Microtops sun photometer) and were calibrated at the NASA Goddard Space Flight Centre (Smirnov *et al.*, 2009). The hand-held Microtops sun photometer has been used across the world since 2004 and are particularly popular on ship-based campaigns due to their ease of use, low cost and portability (Figure 8). These instruments are specifically designed to measure columnar optical depth through five spectral channels and the water vapour content (Smirnov *et al.*, 2006, 2009). The

configuration used within this study was: 440, 500, 675, 870 and 1020 nm and the bandwidths of the interference filters were between 2 - 4 nm. The Microtops sun photometer uses a narrow field of view radiometer that is pointed directly at the sun with a 1° - 3° field of view (Porter *et al.*, 2010). It also has inbuilt temperature and pressure sensors and logs the time and geographic location at the point of measurement. The estimated uncertainty of the optical depth of each channel does not exceed ±0.02 (Porter *et al.*, 2010; Smirnov *et al.*, 2009).

The operator of the Microtops sun photometer must follows a protocol when taking readings with the hand-held instrument. This includes taking 5-6 consecutive scans which takes approximately a minute to complete, and measurements can only be recorded during times the Sun is clear of any visible clouds. It should be noted that it is at the operators discretion as to whether the Sun is cloud free at the time of reading. However an algorithm is utilised during data processing to detect and remove any measurements that are likely to be obscured by clouds. This can also compared with cloud-data instruments such as LiDAR during the correction of the data. If sky conditions permit, the operator should take multiple readings through out the day.

Figure 8: Solar Lights Hand-held Model 540 Microtops II Sun photometer that is used within the this study. The instrument must be directed at the sun whilst there is no cloud coverage, and the Sun Target assists the user to ensure that the instrument is within the field of view (Solar Light, 2020).

2.1.4 LiDAR

The LiDAR instrument that was used on the CAPRICORN II campaign was the Leosphere RMAN 510 Raman UV polarisation LiDAR and was used to provide regular profiles of height-resolved backscatter across the Southern Ocean (Alexander and Protat, 2019). The instrument was primarily used to record cloud properties. LiDAR instruments have a basic transmitter and receiver setup as showing in Figure 9. The instrument transmits short light pulses with lengths of tens of nanoseconds and specified spectral properties that are generated by the laser (Wandinger, 2005). Most systems apply a beam expander within the transmitter unit to reduce the divergence of the light beam before it is directed into the atmosphere (Wandinger, 2005). The telescope acts as the receiver, collecting the photons that have backscattered from the atmosphere. This is followed by a optical analyser which selects specific wavelengths or polarisation states from the light from the received (Wandinger, 2005). The received optical signal is then converted into a an electrical signal through a detector. The height is dependent on the time elapsed between the transmitting and receiving the laser pulse (Wandinger, 2005). The reduction in signal intensity determines the depth and properties of the cloud and aerosol (Wandinger, 2005). The viewing angle of the instrument is also different from the Microtops sun photometer, the LiDAR is directed straight up at the sky and remains in this fixed position for the entirely of the campaign.

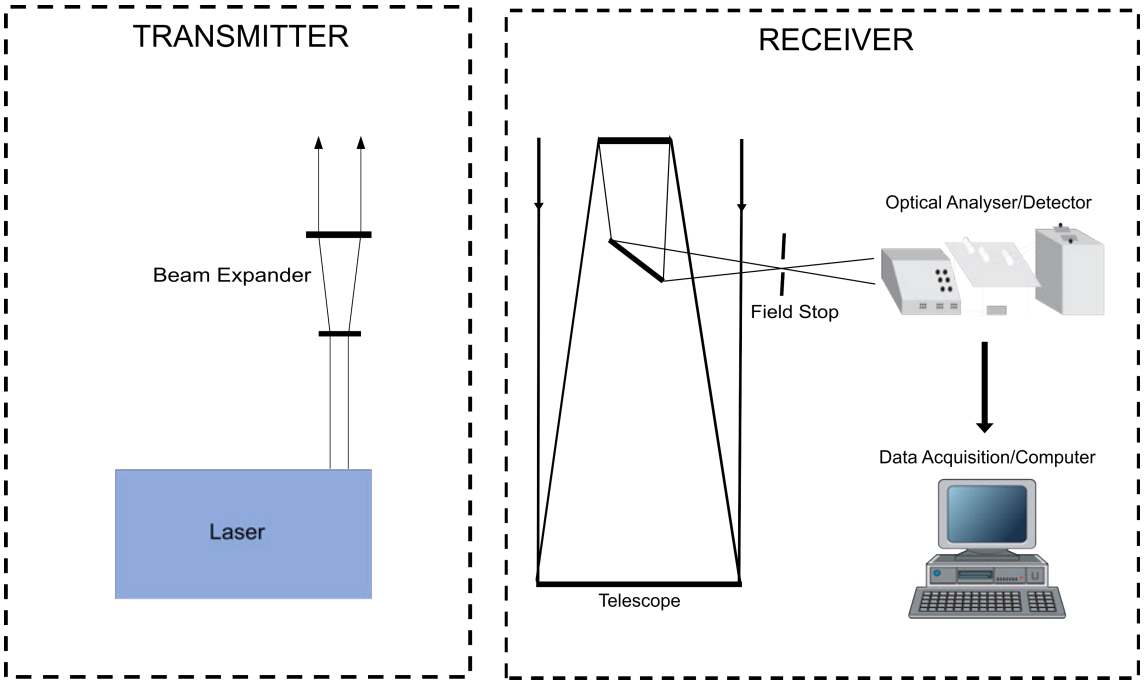

Figure 9: General setup of a LiDAR system. Digitally produced using images sourced from ian.umces.edu (2020). Adapted from: (Wandinger, 2005)

For this campaign, the LiDAR instrument transmits at 355nm, at which it receives elastically backscattered light (referred to as Rayleigh), and at 387 nm, which receives

nitrogen inelastic backscatter (called Raman) and retrieving the vertical distribution of scatterers from both transmitters during the day and night (Alexander and Protat, 2019). The Raman backscatter is three orders of magnitude weaker than the Rayleigh backscatter, however it allows for LiDAR equations to be solved at night time whereas Rayleigh backscatter allows for solving calculations to during both daytime and night time.

2.2 Analytical Methods

2.2.1 Microtops sun photometer data analysis

Data processing, graphing and analysis within this report was conducted through the software 'R' and the graphical interface 'RStudio' (R Core Team, 2019; RStudio Team, 2019). Both programs are open source and were selected as they are commonly used within the atmospheric science community. There are many packages within 'R' that are developed by users which provide useful functions for analysis of large time series such as the package 'openair' (Carslaw and Ropkins, 2012). The 'openair' package was developed for the purpose of analysing air quality and atmospheric composition data, and is particularly well suited to analysing time series and monitoring datasets. A sample of the code that was used for data import and generation of time series and violin plots is presented in Appendix A1.

For this study, the raw and processed data collected by the Microtops sun photometer was analysed. The raw data was supplied by CSIRO for comparison with the filtered dataset that was obtained from the MAN website (Giles and Holben, 2020). When analysing the AOD results that were taken throughout the campaign, there were periods of high AOD results for the area and other periods that were relatively normal when compared to established sites such as Cape Grim. Due to the segmented nature of a data collection process that is dependent of clear skies, the data were analysed using 3 selected periods of the campaign. They identified as Period 1 (January 15^{th} to 16^{th}), Period 2 (January 19^{th} to 20^{th}) and Period 3 (January 30^{th}). These periods were classified as high AOD measurements for Periods 1 and 2 and the low for Period 3 from initial analysis, and each period also has a minimum of 45 observations collected by the Microtops sun photometer. Data collected by the Microtops sun photometer and LiDAR for each period were then analysed using a series of techniques to understand the significant change in AOD throughout the campaign.

2.2.2 LiDAR data processing

To use the LiDAR Rayleigh and Raman data for analysis, a reference value for particle backscatter must first be set at altitude, z_0. The altitude, z_0, that was used for this dataset was 3000 m asl (Alexander and Protat, 2019). The altitude was used as it was well within

the troposphere for the entire data set, a region of the atmosphere that is ideal as scattering is negligible. The altitude chosen for this study would be considered low when compared to the tops of aerosol layers around the world, but within the Southern Ocean nearly all detectable aerosols are confined within the MBL.

Also, due to the biaxial nature of the LiDAR instrument, there is an incomplete overlap between the transmitted laser and the field of view of the receiver; below 0.5 km must be corrected with an overlap function to allow for the partial overlap. The overlap function that was used for this data was implemented with algorithms created by Alexander and Protat (2018). Within the data analysed in this study, only the values within an altitude of 300 m and 3 km were used.

Elastic LiDARs allow for vertical profiles of aerosol backscatter to be calculated by solving the lidar equation. However, AOD cannot be determined independently as the one equation cannot solve two unknowns (Alexander and Protat, 2019). Therefore the lidar ratio $S(z)$ must be assumed by having no aerosol scatter at 3 km (Alexander and Protat, 2019).

The AOD results were derived from the backscatter data using the lidar ratio $S(z)$ and the backscatter. The lidar equation relates to the signal detected to the backscattering coefficient as a function of distance (Josset *et al.*, 2008). To integrate the column or partial column to get AOD, the following equation was used:

$AOD = \sum \beta \times \triangle x$

Where β is the backscatter ($m^{-1}.sr^{-1}$), and $\triangle x$ is the difference in grid size of altitude (m). In this dataset, the altitude goes up by 15 m each step. For every step that the laser transmits and recieves (30 m) its takes 1.00e-7 seconds.

2.2.3 Backward Trajectories

Finally, analytical backward trajectories were created for each period as they can provide vital information of the origin of the observed aerosols and the patterns that may correspond with the measurements recorded. Within this study, 3 day back trajectories were created for the periods of interest using the Hybrid Single-Particle Lagrangian Integrated Trajectory (HYSPLIT) model (Draxler and Hess, 1998). The HYSPLIT model uses meteorological data that is produced by the National Weather Service ETA model to compute the dispersion of air parcels (Draxler and Hess, 1998). The HYSPLIT model was used to generate 3-day back trajectories for air parcels arriving to the ships coordinates at the time of the last Microtops sun photometer measurement collected in the given period, this process conducted was for all three study periods.

Part III

3 Results and Discussion

For this report, the results and discussion was divided into four sections.

Firstly, the processing and the filtering procedures conducted by MAN on the Microtops sun photometer dataset were analysed to determine the extent of data filtration and correction.

Secondly, an overview of the results collected during the CAPRICORN II campaign were compared with AOD measurements collected at Cape Grim's BAPS and established stations surrounding Antarctica. This comparison was used to determine the change in AOD measurements throughout the campaign and identify periods of high and low readings.

Then a comparison between the Microtops sun photometer AOD dataset with the LiDAR derived estimated AOD measurement was graphically presented to determine comparability of the datasets. If the data collected by the instruments are comparable, the amount of data that can be analysed will increase significantly as the LiDAR is continuously collecting measurements throughout the day and night.

Finally, a case study comparing three periods of high and low AOD measurements within the campaign were analysed separately before being compared statistically together.

3.1 Analysis of the processing and filtering procedure conducted by the Maritime Aerosol Network

Initially, a comparison between the raw (grey circle) and processed (orange triangle) AOD data was conducted to determine the level of filtering was conducted by MAN when correcting the Microtops sun photometer data as shown in Figure 10. The raw dataset is the raw values that are collected by the Microtops sun photometer instrument. The processed AOD data has undergone correction and filtering by MAN. The filtering and correction process conducted by MAN was reviewed in the Introduction of this report and is available on their website (Smirnov *et al.*, 2009).

Overall, most of the raw data appears to have had a calibration standard applied to it as the raw data is approximately 0.2 greater than the corrected processed dataset. Adding a calibration standard prior to campaign is standard practice as it allows for adjusting for the any error or offset that the instrument may experience during the voyage and to correct within the dataset during processing (Smirnov *et al.*, 2009). An offset may also be intentionally set within the instrument as to prevent any negative AOD values from being measured as it is impossible to have negative AOD.

The analysis showed that whilst the data was corrected, it was not heavily filtering as initially assumed. Overall, the data had been calibrated, correcting the value of AOD,

and only 6 points were removed from the initial raw AOD dataset. These 6 points have been highlighted within Figure 10. These points were removed as they were outliers with extremely high optical depths in comparison to the other points measured at the time. These were likely caused through operational error such as cloud moving over the instruments field of view during the measurement.

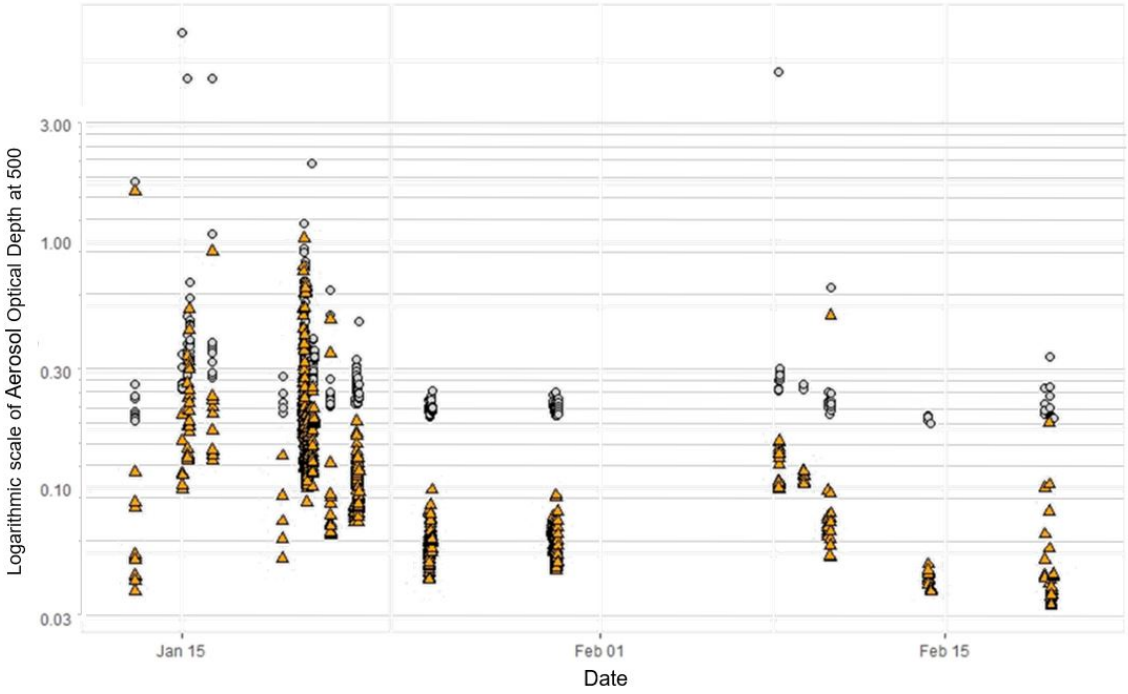

Figure 10: Comparison of raw (grey circle) and filtered (orange triangles) AOD results recorded at 500 nm. The data points were collected by a Microtops sun photometer during the CAPRICORN II campaign in January and February of 2018.

3.2 Microtops II sun photometer Aerosol Optical Depth

Following the filtering analysis, violin plots were also produced to determine the distribution of AOD measurements throughout January and February and were compared with data collected during these months at Cape Grim between 2014 and 2018. The violin plots also incorporate box plots to depict the median, maximum, minimum and interquartile range. The processed AOD measurements for the campaign were then analysed in the analysis and it was found that there were significantly and consistently higher measurements recorded during the first week of the campaign in comparison to the rest of it (Figure 10). During CAPRICORN II, AOD measurements with a wavelength of 500 nm had a overall mean of 0.129, a median of 0.105 and reaching a high of 1.607 overall.

There is a significant shift in the distribution of the measurements when comparing the measurements taken in January to February. Violin plots of each month a presented in Figure 11 and although both months are positively skewed, the measurements taken in January are more uniform, with a median of 0.116. February however has a very

positively skewed logistic distribution, with a median of only 0.047.

To understand how these measurements compared to what has been found in the region, a series of violin plots of of the measurements found during the voyage were compared to those collected at the permanent site on Cape Grim, Tasmania are also presented in Figure 11. The AOD measurements were graphically presented by month, January (1) and February (2), and location, CAP II and Cape Grim.

When comparing these distributions to the AOD measurements that were taken at Cape Grim, Tasmania (Figure 11) between 2014-2018 for January and February, there was a notable shift in the mean and median readings. Both months had positively skewed distributions, with January resulting in a range of medians between 0.059 to 0.081 during the 5 year period, almost half of AOD measured whist on the ship. For February, Cape Grim measured higher AOD than what was recorded on the ship, with AOD medians recorded between 0.062 to 0.107.

It is important to note that the AOD measurements that were collected at Cape Grim were from a stationary site that is situated at a latitude of 40.68°S, whilst the ship recorded measurements between 46.17°S and 63.87°S. As Cape Grim and the measurements taken during CAPRICORN II experience multiple atmospheric circulation cells, specifically the uplift between the Ferrel and Polar cells at the polar front located at 60°S (Figure 4), the sites could experience slightly different AOD measurements.

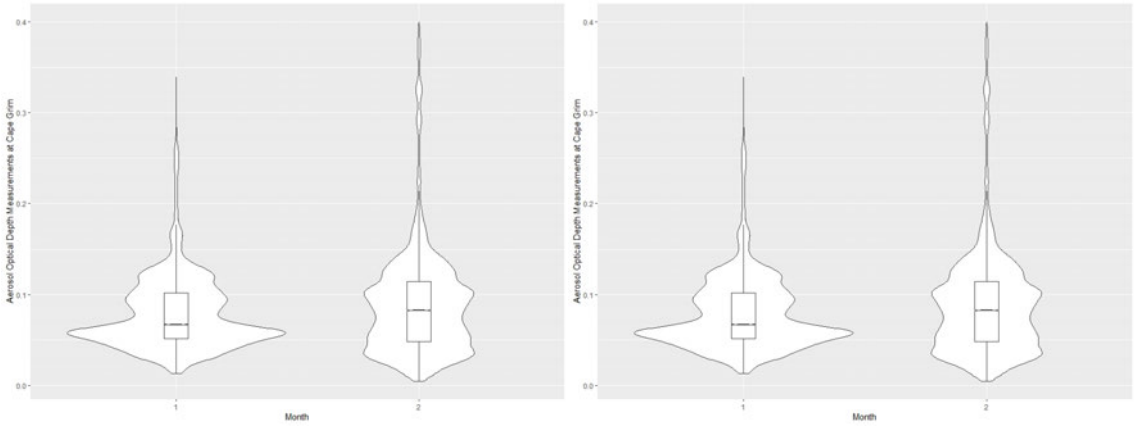

Figure 11: Comparison of the Filtered AOD measurements collected by the Microtops sun photometer in January (1) and February (2). Distribution of AOD measurements collected in January (1) and February (2) at Cape Grim, Tasmania in 2014-2018.

The averaged AOD measurements can also be compared to other multi-year studies that have been collected at coastal sites around Antarctica. Chaubey *et al.* (2011) collated a series of averaged AOD measurements collected between 1969 through to 2008 from within Antarctica (Table 2). Across three studies that also measured AOD at 500 nm, the highest optical depth measurement was 0.044, which was a third of the average AOD (0.129) measured during the CAPRICORN II campaign.

Table 2: Antarctica stations, location, features and measured AOD at wavelength of 500 nm. Features of the site are labelled C - Coastal and LA - Low Altitude. Adapted from Chaubey *et al.* (2011)

Station Name	Type	Country	Location	AOD	Year	References
Maitri	C, LA	India	71°S, 12°E	0.034 ± 0.005	2007-2008	Chaubey *et al.* (2011)
Larsemann Hills	C, LA	India	69°S, 76°E	0.032 ± 0.006	2007-2008	Chaubey *et al.* (2011)
Terra Nova Bay	C	Italy	76°S, 164°E	0.01 - 0.0	2005	Tomasi *et al.* (2007)
Neumayer	C, LA	Germany	71°S, 8°W	0.044	1999-2002	Weller *et al.* (2008)
Mirny	C, LA	Russia	67°S, 93°E	0.03	2006	Tomasi *et al.* (2007)

3.3 Estimated AOD derived from LiDAR comparison with Microtops AOD

As an estimation of AOD can be derived from LiDAR, it was important to understand how comparable the dataset would be to the measurements taken using the Microtops sun photometers. Initially, just January 20th 2018 (UTC) was observed as it was the day with the highest proportion of Microtop sun photometer readings were taken. A series of vertical profiles showing the retrievals and altitude of the aerosol were created during the periods of Microtops measurements. The data was interpolated down from an altitude of three kilometres as it was assumed that there were no aerosols at that point.

In Figure 12, the estimated AOD derived from the LiDAR backscatter data is presented in four consecutive two minute intervals. The vertical profiles at 12:00 and 14:00 show sensible partial backscatter measurements, depicting much of the aerosol to be between 0.3 to 1 km in altitude. However, the profiles are times 00:10 and 00:14 were meaningless. The levels of noisiness was continuously throughout the dataset.

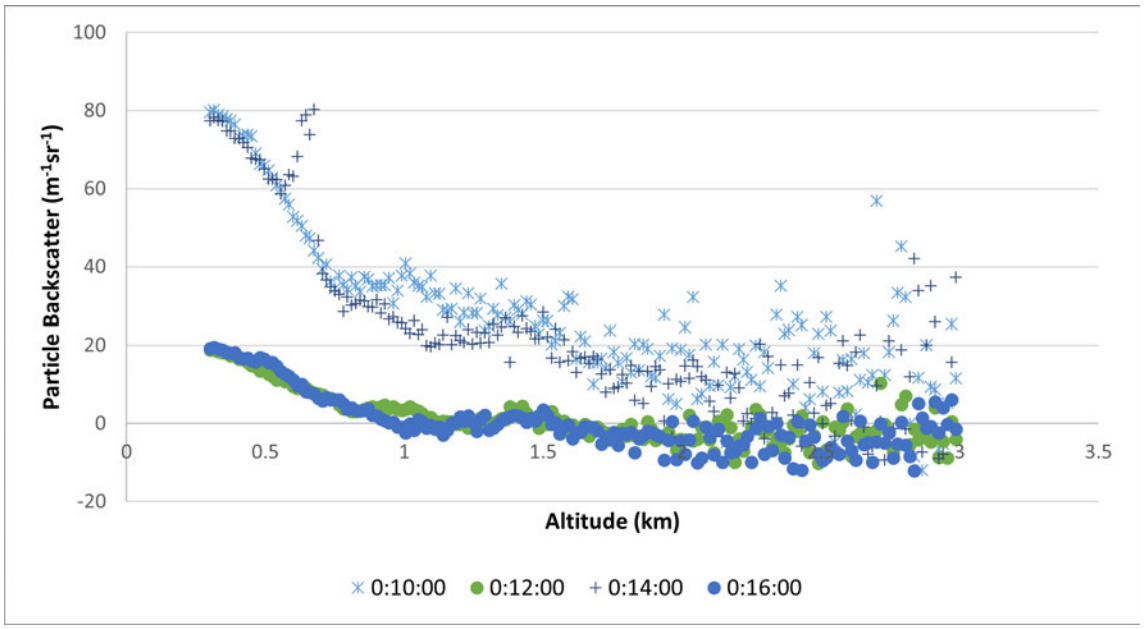

Figure 12: Vertical profiles of particle backscatter collected from LiDAR between 00:10 to 00:16 on January 20th, 2018 at 355 nm.

The derived AOD measurements for the day-time and night-time were then graphed alongside the measurements taken by the Microtops sun photometer for the total campaign period (Figure 13). The day-time derived AOD was significantly noisier than the Microtops sun photometer AOD when compared to the AOD collected at night-time. This is likely due the amount of light that is present in the sky during the day. As LiDAR measure the difference intensity of the laser it transmits and receives to determine aerosol backscatter, the additional sunlight is likely to create extra noise within the data. The readings taken at night were much more sensible as there was no extra light causing meaningless data.

Although the night-time AOD measurements were not used within this report, was comparable to the results that were found by the Microtops sun photometer. This could allow for a much larger dataset of AOD to be analysed, as data can be collected continuously at night and be collected from LiDAR datasets collected during other campaigns.

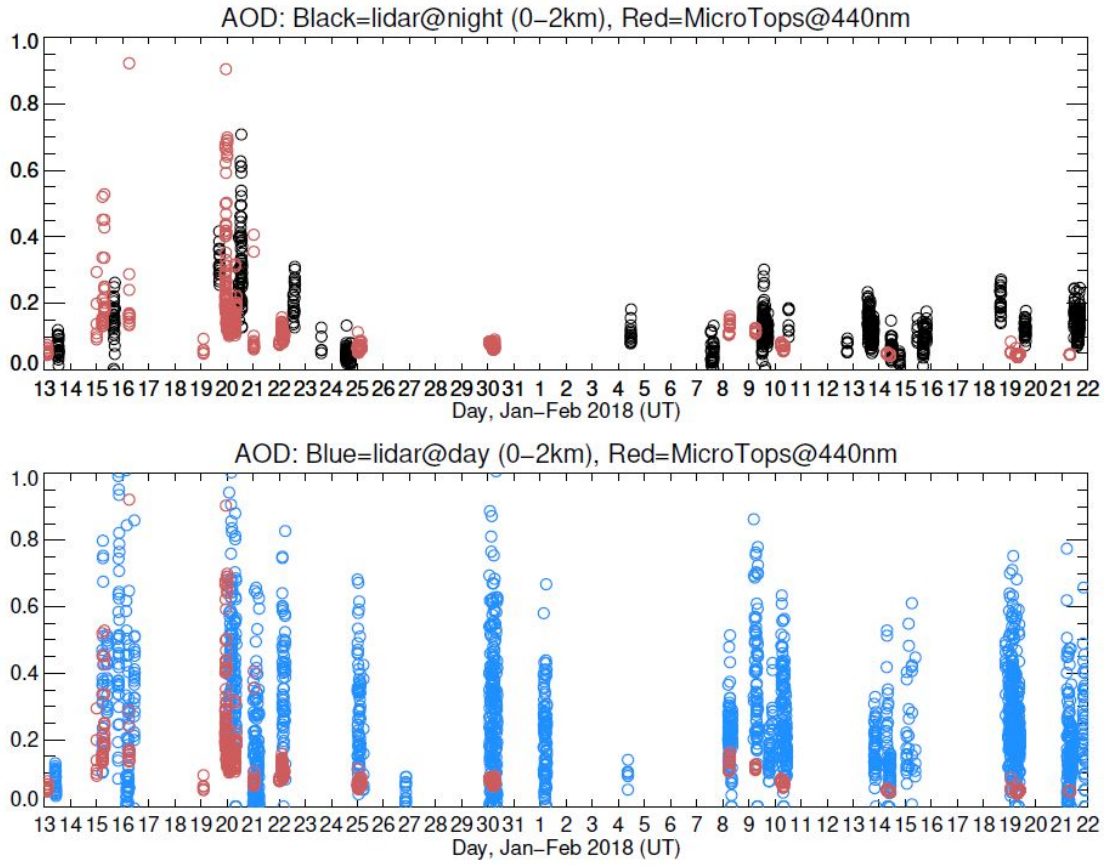

Figure 13: The derived AOD collected by the LiDAR at night-time (black) and day-time (blue) is compared to the AOD collected by the Microtops sun photometers (red) for the entire campaign. The wave length of the derived AOD was 380 nm (S. Alexander, 2020).

3.4 Case study analysis of high and low periods of AOD measurements during the CAPRICORN II campaign

In order to understand the distinct and continuous periods of high and low AOD readings that were recorded during the campaign, three case studies were explored. The case studies consisted of three periods, with Periods 1 and 2 portraying high AOD measurements and Period 3 representing the low AOD measurements taken. To determine what the cause of the high AOD readings, three periods of the campaign were studied and compared across instruments.

3.4.1 Period 1 of high AOD measurements

The first period observed was 33 hours long, from 00:00 January 15th to 09:00 on January 16th, 2018 (UTC) as presented in Figure 14. Period 1 is identified as one of the high AOD case studies. Within this period, 45 observational measurements were taken and filtered by MAN. This period of the campaign had the some of the highest AOD readings

collected throughout the study and all measurements were collected between latitudes 46.650°S and 48.00°S. Overall there was an mean optical depth of 0.22, a median of 0.180 and a maximum value of 0.921.

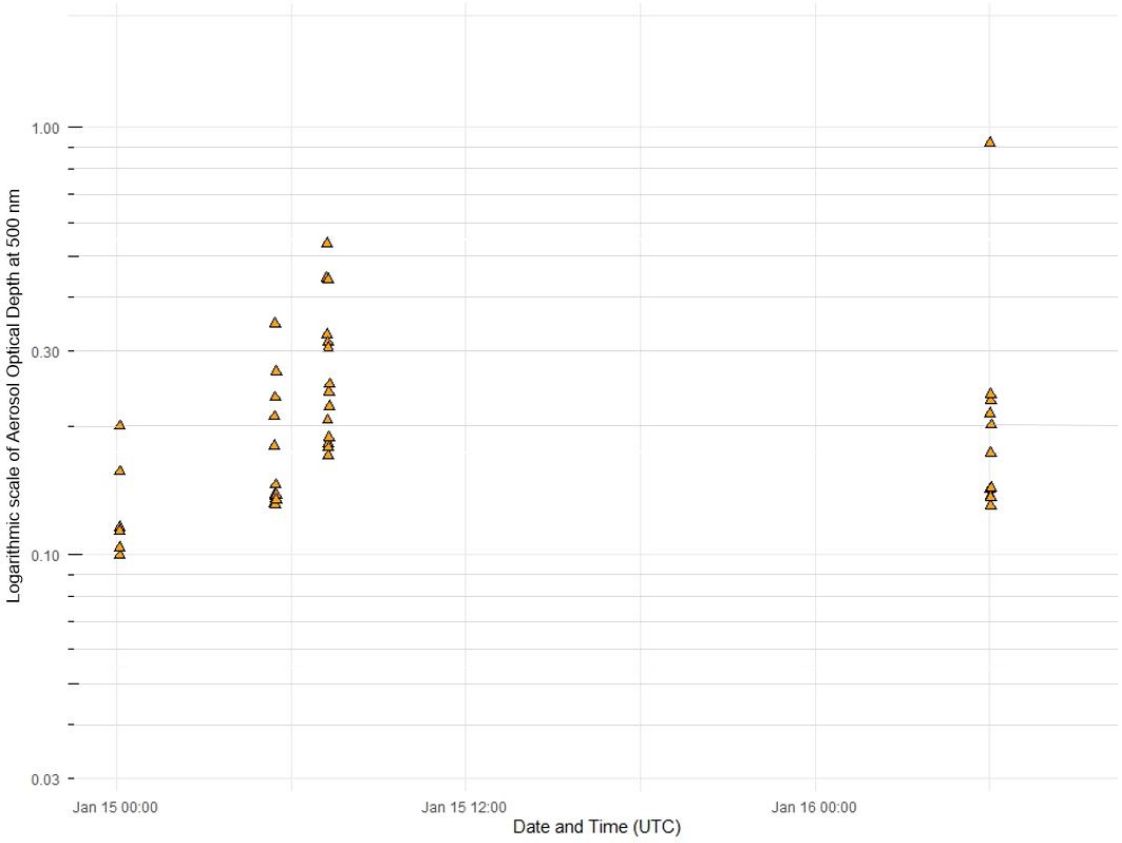

Figure 14: The first study period was 33 hours long, between 00:00 January 15th to 09:00 on January 16th 2018 (UTC).

To determine if there were any filtering or operational errors, LiDAR can be used to determine if there were any clouds present, where the aerosols are in the vertical profile in the sky at the time of measurements. In Figure 15b) and d) the clouds have been classified over a 48 hour period. Throughout the 15ththere was a patchy low-level cloud, labelled liquid water (LW) in the figure, in the well mixed, MBL throughout the 24 hour period. However, during the times that the AOD was measured by Microtops sun photometers there appear to be no LW present, specifically between approximately 5:00 to 6:30UTC, during which the majority of AOD measurements for were recorded (Alexander and Protat, 2019). Similarly, on January 16th there was patchy LW present for much of the day excluding the approimately 04:30 to after 06:00, during which the Microtops measurements were collected. It is clear to see where the LiDAR measurements become too noisy as the readings transition from solid colour to static above the base of the cloud bottoms, as shown in Figure 15 c) between 00:00 to 03:00. This can be used to assess where the aerosols are within the vertical profile. For this period, aerosols are confined within the MBL (>1.5 km altitude), with weak backscatter (Figure 15a and c) above the

inversion top (Alexander and Protat, 2019).

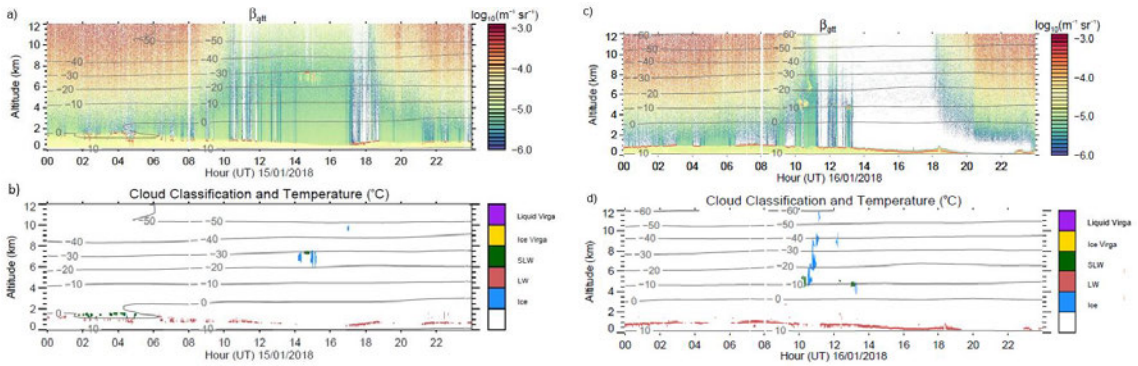

Figure 15: LiDAR results and output of the aerosol and cloud detection algorithm from January 15th, 2018 and January 16th, 2018 (UTC). a) and c) The calibrated attenuated backscatter signal β_{att} (logarithmic scale, units of $m^{-1}sr^{-1}$); b) and d) cloud classification and temperature interpolated from the the ERA-Interim reanalysis (lines, units of °C) where SLW is supercooled liquid water and LW is liquid water (S. Alexander, 2020).

The aerosols that have been recorded could be transported from land-locked areas, high attitudes of the the ships voyage path itself. Therefore, the NOAA HYSPLIT model was utilised to calculate the backward trajectories and assist in identifying the source of the polluted aerosols. This model has been used within a variety of studies observing aerosols from around the world (Liu *et al.*, 2017). The 72 hour backward trajectories were utilised to calculated the source of the aerosols at the observational sites at the start, 00:00UTC on January 15th 2018, and the end, 07:00UTC on January 16th 2018, of the period as shown in Figure 16. The model was also used calculated 6 backward trajectory (coloured lines) and wind path every 4 hours (each new shape on the line). As observed on the backward trajectories in Figure 16, the wind patterns were fairly similar throughout the entire period, with all trajectories moving from West to East across the Southern Ocean and within the lower 500 meters of the atmosphere and at sea level for the last 48 hours of the back trajectory. For all wind paths, the wind speed gradually reduced as it reached it the ship. This is particularly clear to see in the green, dark blue and red backward trajectories ending on January 16th. The last 48 hours of each wind path shows the wind moving at a significantly slower wind speed as the circles, squares and triangles are measured closer together over time.

As there are no land or sea ice masses across the trajectory path and the wind patterns were quite fast and low in altitude to the oceans surface for a prolonged period of time, sea spray production is likely to be may encourage mass sea spray (Merkulova *et al.*, 2018).

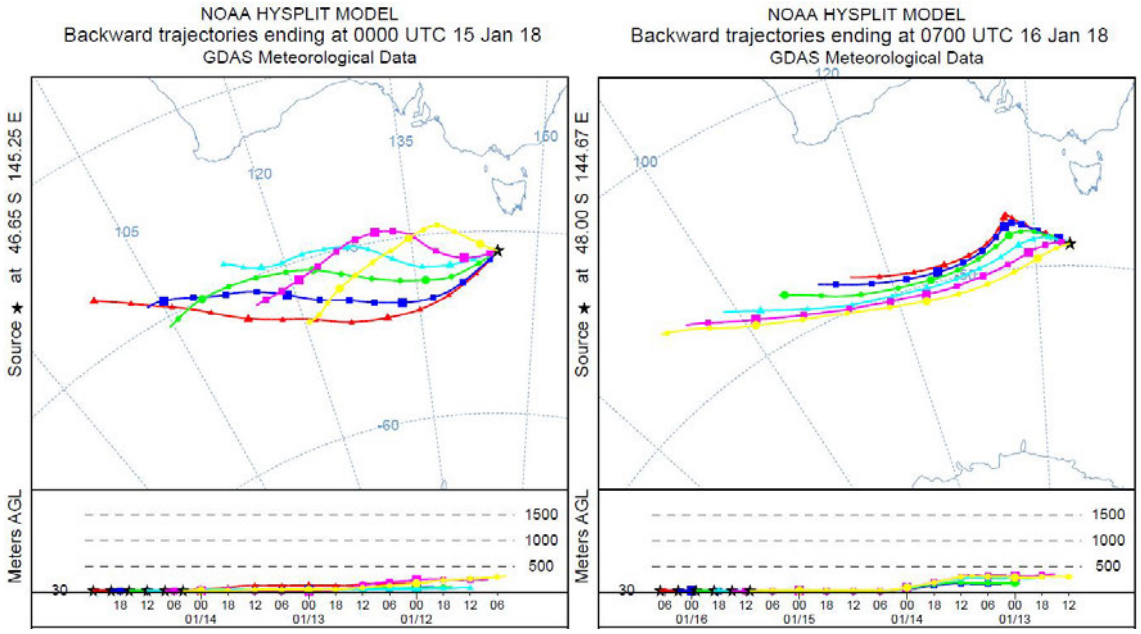

Figure 16: Period 1 backward trajectories ending at the RV *Investigators* starting location (star at 46.65°S, 145.25°E) at 00:00UTC on January 15th 2018 and ending location (star at 48.00°S, 144.67°E) at 07:00UTC on January 16th 2018 (UTC), respectively. The backward trajectory duration was 72 hours.

3.4.2 Period 2 of high AOD measurements

The second period observed within this study was 12 hours long, from 22:00 January 19th to 10:00 on January 20th, 2018 (UTC) as presented in Figure 17. Within this period, 259 observational measurements were taken and filtered by MAN. This period of the campaign showed had highest density of measurements taken over any day of the campaign, with consistently high results. The average AOD measurements that was recorded was 0.198, the median was 0.155 and the maximum value recorded was 1.04, the second highest measurement taken throughout the entire period.

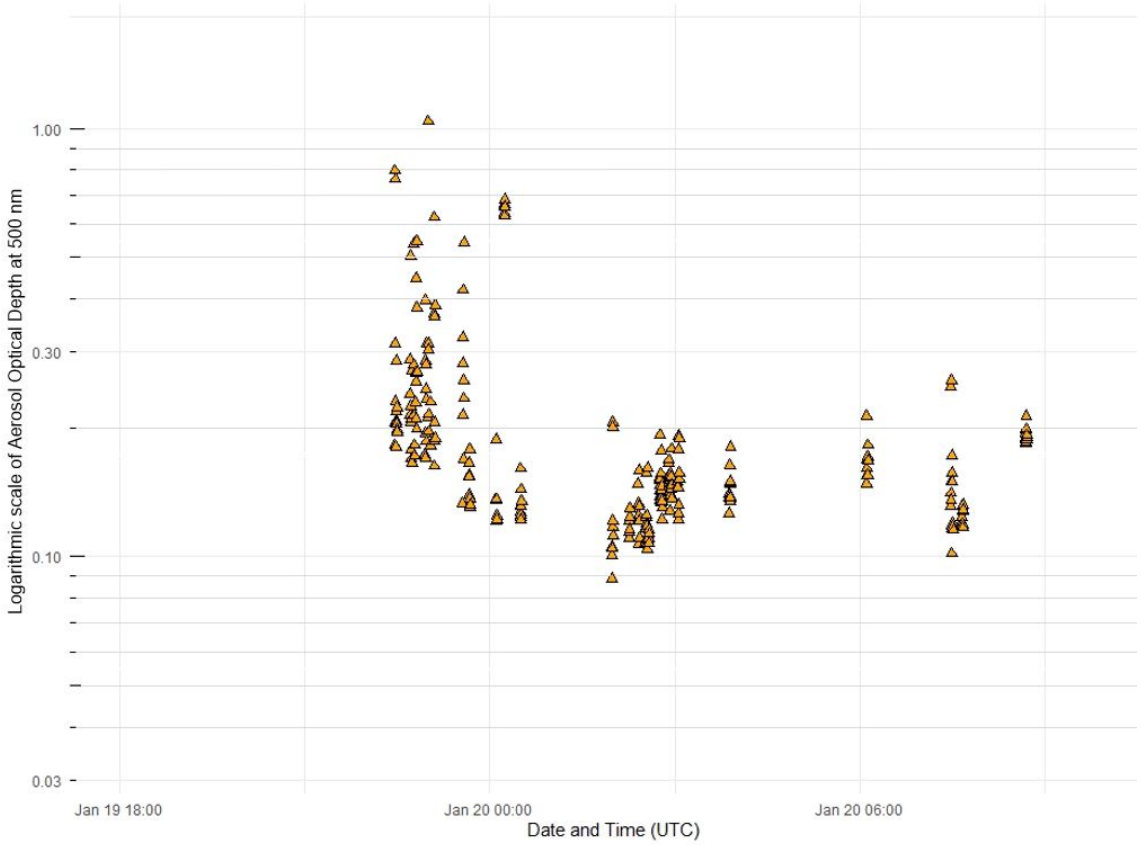

Figure 17: The second study period that was reviewed was 12 hours, occurring between 22:00 on January 19th through to 10:00 January 20th 2018 (UTC).

Period 2 experienced similar conditions to what was found in the Period 1 LiDAR results. As shown in Figure 18, there was low altitude, sparse patchy low level clouds present between 22:00UTC on January 19th through to approximately 01:30UTC on January 20th, and again from 05:30 to 06:30UTC on the same day. These times do coincide with some of the measurements taken on using the Microtops sun photometer. However, it should be noted that due to the different angle of field of view of each instrument, that there may have been no clouds in front of the sun when taking measurements, whilst there were some directly above the LiDAR viewer. This is likely due to the sparseness of the cloud recorded but also as there was very little change in AOD results during the three hours of measurements between 01:30 and 04:30UTC where there were no clouds present in the LiDAR data and 104 measurements were recorded using the Microtops sun photometer. The backscatter plots (Figure 18a) and c)) shows well mixed MBL throughout the entire measuring period (Alexander and Protat, 2019). The backscatter measurements were also moderately low, ranging between -4.0 - -5.0 $\log_{10}(m^{-1}sr^{-1})$ throughout the period.

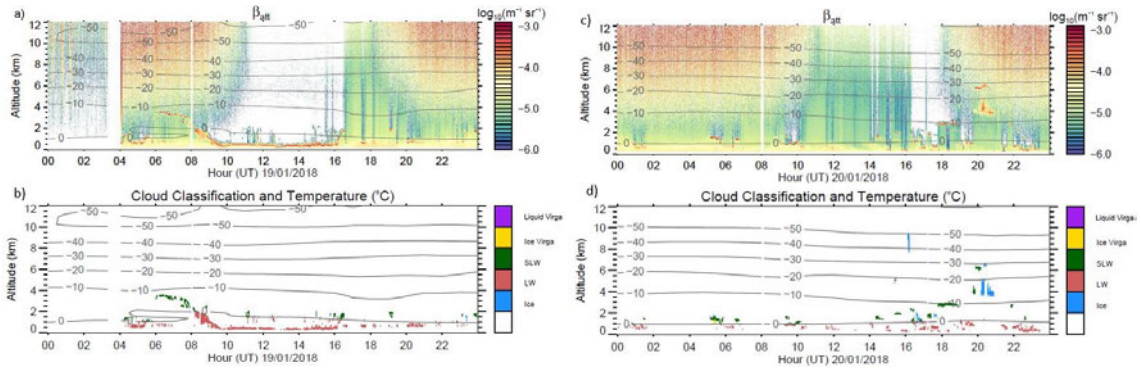

Figure 18: LiDAR results and output of the aerosol and cloud detection algorithm from January 19th, 2018 and January 20th, 2018 (UTC) respectively. a) and c) The calibrated co-polarisation backscatter signal β_{att} (logarithmic scale, units of $m^{-1}sr^{-1}$); b) and d) cloud classification and temperature interpolated from the the ERA-Interim reanalysis (lines, units of °C) (S. Alexander, 2020).

In Figure 19, the six 72 hour back trajectories were produced using the NOAA HYSPLIT model ending at the location of the RV *Investigatory* on 09:00UTC on January 20th 2018. The light blue track is the most similar to the time and position of the inital starting point of Period 2, encompassing the completed period on one backward trajectory map.

Throughout the 24 hours observed, the westerly wind travelled consistently along the 50 S latitude with only slight variation northwards and entirely at sea surface level. The wind speed remained relatively consistent for the first 3 wind paths (yellow, pink and light blue), before increasing in speed for the remaining three paths. Similarly to Period 1, these characteristics suggest the encouragement of mass sea spray production with no sea ice present in the wind path to prevent interaction with the ocean waves (Merkulova *et al.*, 2018).

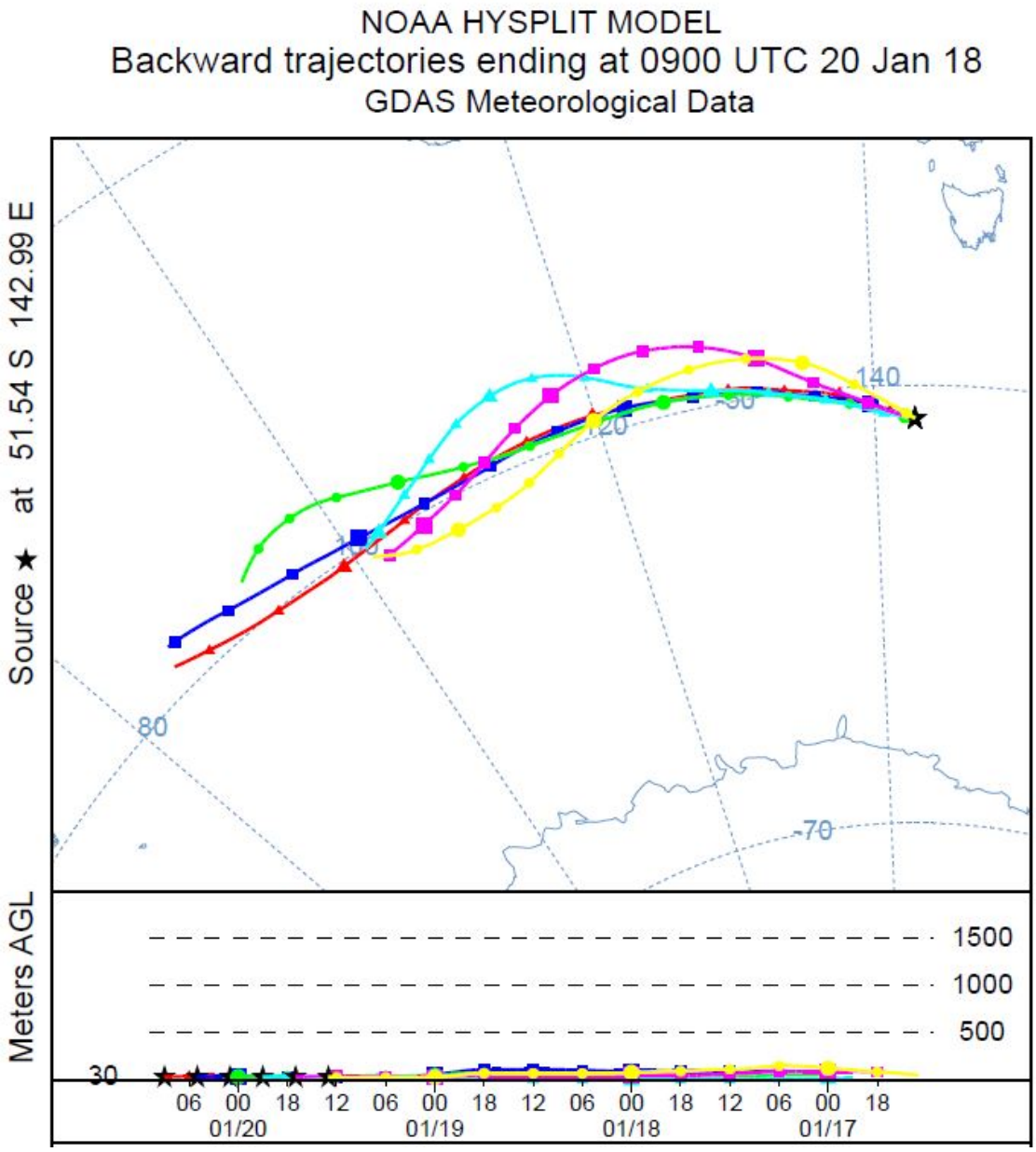

Figure 19: Period 2 backward trajectories for the ending location (star at 51.54°S, 142.99°E) at 07:00UTC on January 20th 2018 (UTC). The backward trajectory duration was 72 hours.

3.4.3 Period 3 of high AOD measurements

The final period observed was 9 hours long, from 00:00 to 09:00 on the January 30th 2018 (UTC) as presented in Figure 20. Within this period, 119 observational measurements were taken and filtered by MAN. This period of the campaign was similar to the remainder of the voyage in presenting what is considered normal readings for the area. For the period, the average AOD measurement was 0.061, the median was 0.059 and the maximum value was 0.095.

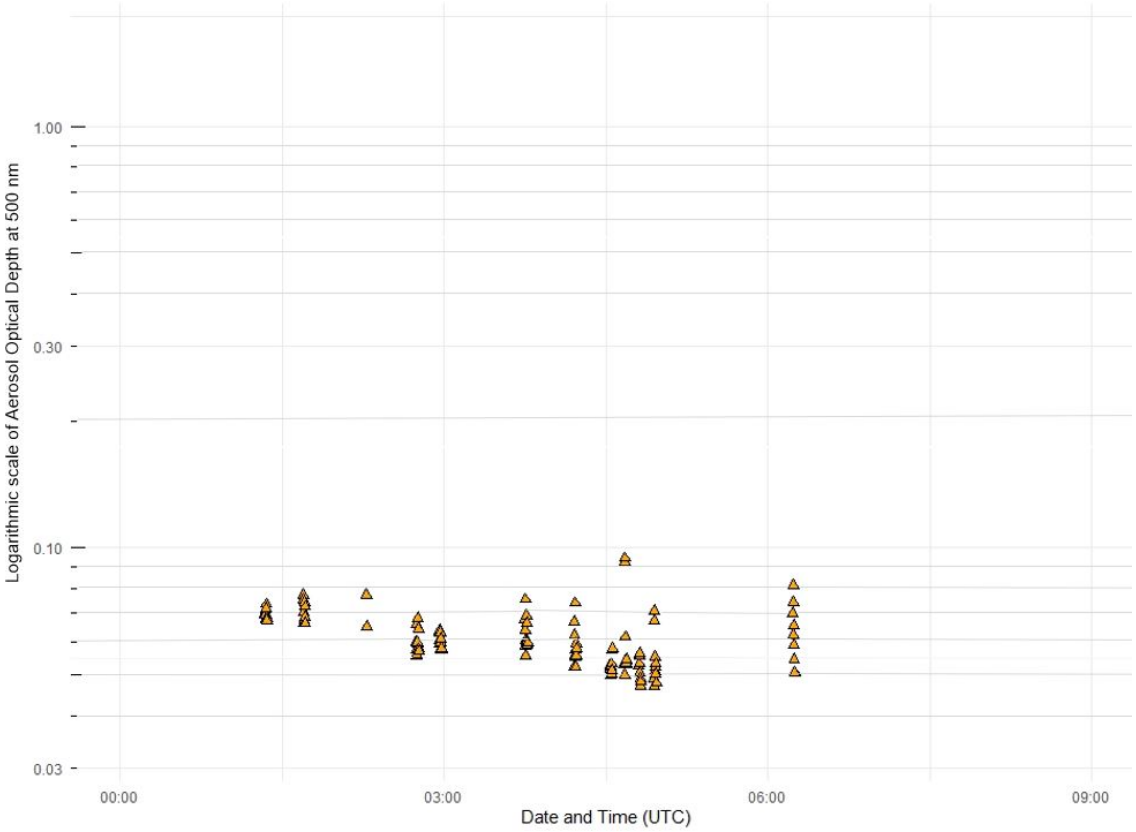

Figure 20: The final study period that was reviewed was 9 hours long, occurring between 00:00 through to 09:00 on January 30th2018 (UTC).

As shown in Figure 21b) there were no clouds present during the measurement collection times for Period 3, although there was significant ice present after 09:00 UTC. The first measurement for this period was taken at 01:20 UTC and there is weak but well mixed backscatter present from approximately 1:30 to 09:00 UTC up to an altitude of 2 km. This was also the lowest backscatter measurements of all the periods, ranging between -4.5 - -5.5 $\log_{10}(m^{-1}sr^{-1})$ throughout the period.

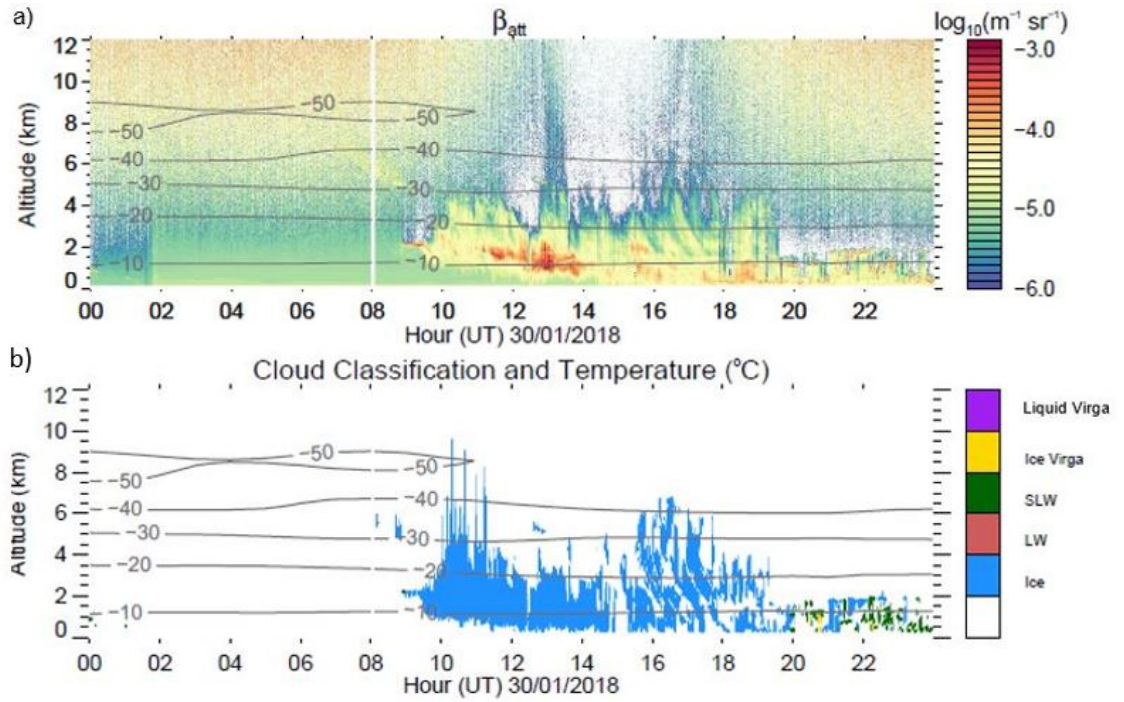

Figure 21: LiDAR results and output of the aerosol and cloud detection algorithm from January 30th, 2018(UTC). a) The calibrated co-polarisation backscatter signal β_{att} (logarithmic scale, units of $m^{-1}sr^{-1}$); c) cloud classification and temperature interpolated from the the ERA-Interim reanalysis (lines, units of °C) (S. Alexander, 2020).

The back trajectories that were produced for Period 3 (Figure 22) were the most dynamic in comparison to trajectories that were produced for Periods 1 and 2. Firstly, the wind travelled between 70°S and 63°S towards the the ship from the south east, which is directed by the Polar easterlies as described in Figure 4. Much of the trajectory path was over land and sea that is covered by ice, with the wind across 2500 meters AGL for the first 48 hours of the back trajectory and lowering to sea level at approximately 11:00UTC on January 29th, 2018. This coincided with the when the individual paths had travelled passed the land and reached the ocean as indicated by the 6 hourly time stamps on each path (Figure 22). The wind speed remained consistently high during the 72 hour period, slowing The increased altitudes and wind paths over land and sea ice indicated by the back trajectories suggests that the conditions were not suitable for the production of sea spray aerosol production, resulting in lower AOD as measured by the Microtops sun photometer and the LiDAR (Figures 20 and 21) (Merkulova *et al.*, 2018).

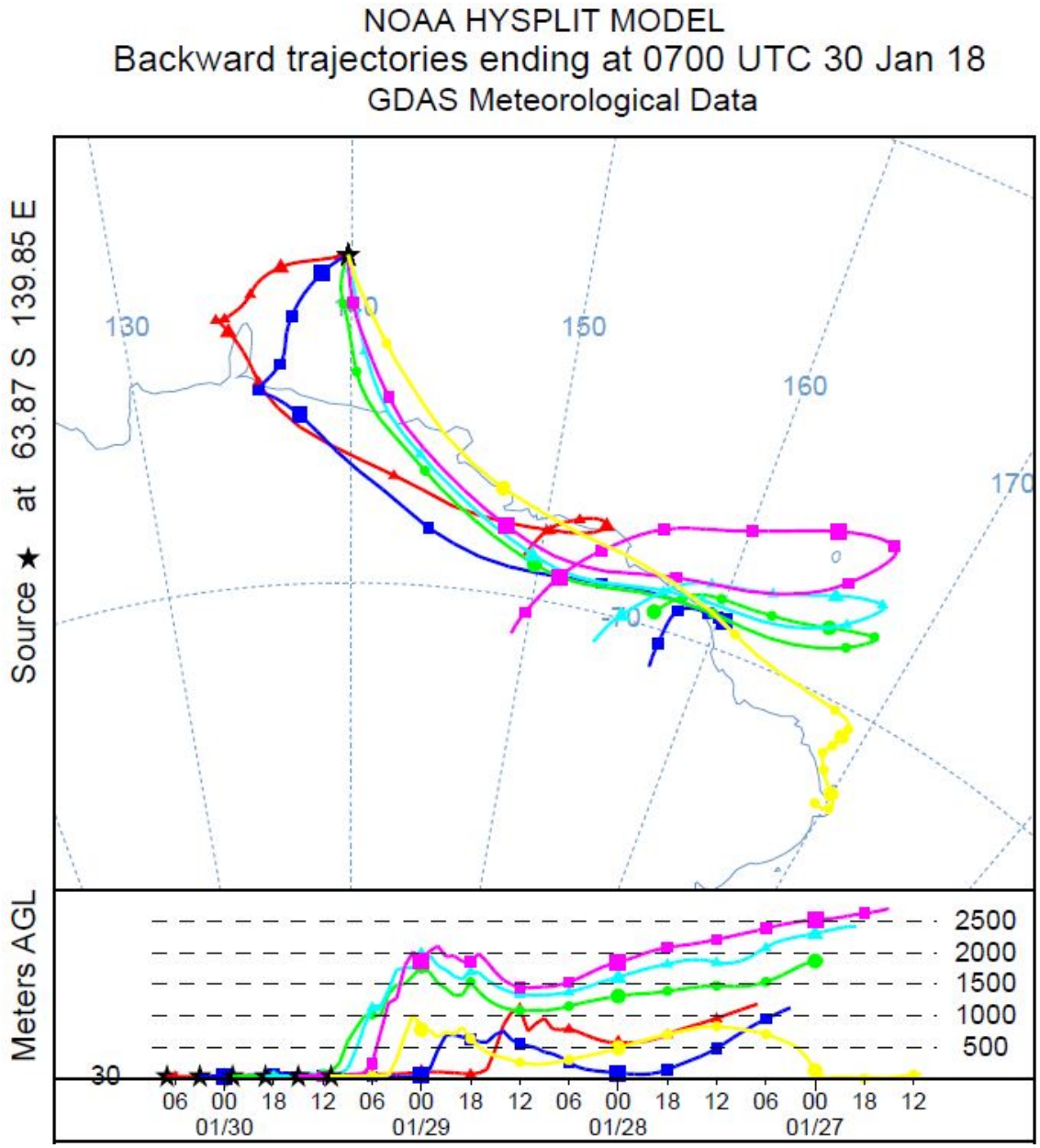

Figure 22: Period 3 backward trajectories for the ending location (star at 63.87 S, 139.85 E) at 07:00UTC on January 30th 2018. The backward trajectory duration was 72 hours.

3.4.4 Physical and statistical analysis between the high and low periods

Overall, Periods 1 and 2 displayed very similar physical mechanism and measurements. They had similar means of 0.22 and 0.198 for Period 1 and 2 respectively. Both periods had back trajectories that remained very low to the oceans surface, initially higher wind speed that slowed 24 hours before reaching the ship were westerly in direction over open ocean. They had some SLW present during the measurement day, although none was present during the AOD measuring periods. Finally, each had well mixed and medium to moderately low backscatter reading within the MBL layer.

The low Period 3 had very different mechanisms acting within the atmosphere at the

time of the measurement period. The period had a mean of Finally, to determine if there is actually any significant difference between the three period, exactly half of the AOD found during Period 1. There was no SLW present in at any point during the measurement day, and there were no clouds during the measurement period. However, there was a lot of ice present in the atmosphere after the measuring period ended. The backward wind trajectory were much faster than what was shown in Periods 1 and 2, with the wind paths reaching altitudes of 2500 m agl (Figure 22). Finally, the attenuated backscatter was well mixed, but the lowest of any period.

To determine if there is any significant difference statically between the high and low periods, a T Test was conducted between each of the periods using the AOD datasets collected. It was found that there was no significant difference between Periods 1 and 2 ($t = 0.651$, $df = 9.214$, $p = 0.531$). However, when the Period 1 was compared to Period 3 it was found to be statistically significantly different ($t = 2.477$, $df = 9.002$, $p = 0.03518$) as the p-value was less than 0.05. Finally, Period 2 and 3 were also found to be statistically significantly different ($t = 16.655$, $df = 263.11$, $p < 2.2e\text{-}16$). Although the T-test only shows a statistical significance, the added similarities found within the LiDAR data and back trajectories suggests that the high AOD periods had the same aerosol type in the atmosphere at time of measurement.

Part IV

4 Conclusion

Measuring aerosols across the Southern Ocean is still as relatively young study within the atmospheric science. However, the importance of understanding and modelling aerosols natural and anthropogenic impact upon climate and is only increasing in importance. Allowing for valuable measurement opportunities by measuring AOD at night-time using instruments like LiDAR can immediately increase datasets by 12 hours, a period of the that was previously inaccessible. This would allow for greater aerosol and climate modelling opportunities as there would be a greater dataset to determine the normal and abnormal AOD measurements and to compare with other physical parameters such as local wind speed and direction, ocean temperature and sea ice.

The filtering and correction processes that was conducted by MAN on this dataset was found to be extremely sensible, resulting in only 6 points that were removed as outliers. However, this resulted in an extremely dynamic series of AOD measurements for the campaign. The was an indication of similar physical parameters causing the high AOD measurements during Periods 1 and 2, including higher wind speeds and no sea ice in wind path, that could have resulted in the formation of sea spray particulates. When compared to what was found within the back trajectory and LiDAR datasets for Period 3, it suggests that no sea spray aerosol formation parameters were present and the AOD measurements for the period.

However, there is still many unknowns within aerosol formation production, especially in this region. Future directions for this project include a future analysis and comparison between AOD collected by Microtops sun photometer instruments and LiDAR, specifically at night-time. Secondly, investigating other physical parameters and mechanisms such as ocean water temperature, satellite imagery at time of collection and wind speed may allow for increased understanding in aerosol formation within the Southern Ocean.

References

Alexander, S. P. and Protat, A., (2018). 'Cloud Properties Observed From the Surface and by Satellite at the Northern Edge of the Southern Ocean.' *Journal of Geophysical Research: Atmospheres*, vol. 123(1), pp. 443–456. ISSN 2169-8996. doi:10.1002/2017JD026552.

Alexander, S. P. and Protat, A., (2019). 'Vertical Profiling of Aerosols With a Combined Raman-Elastic Backscatter Lidar in the Remote Southern Ocean Marine Boundary Layer (43–66°S, 132–150°E).' *Journal of Geophysical Research: Atmospheres*, vol. 124(22), pp. 12 107–12 125. ISSN 2169-897X, 2169-8996. doi:10.1029/2019JD030628.

Ansmann, A. and Muller, D., (2005). 'Lidar and Atmosphere Aerosol Particles.' In: 'Lidar: Range-Resolved Optical Remote Sensing of the Atmosphere,' pp. 105–141. Springer Science+Business Media Inc., New York, NY, 1st edn. ISBN 0-387-40075-3.

Ayers, G. P., Cainey, J. M., Gillett, R. W. and Ivey, J. P., (1997). 'Atmospheric Sulphur and Cloud Condensation Nuclei in Marine Air in the Southern Hemisphere.' *Philosophical Transacations fo the Royal Society B: Biological Sciences*, vol. 352(1350), pp. 204–211. doi:10.1098/rstb.1997.0015.

Brooks, D. R., (2008). 'Instrument Design Principles II: Sun Photometers.' In: 'Bringing the Sun Down to Earth,' pp. 71–96. Springer, Dordrecht, Netherlands. ISBN 978-1-4020-8694-6.

Carslaw, D. C. and Ropkins, K., (2012). 'Openair — An R Package for Air Quality Data Analysis.' *Environmental Modelling & Software*, vol. 27-28(0), pp. 52–61. ISSN 1364-8152. doi:10.1016/j.envsoft.2011.09.008.

Chaubey, J. P., Moorthy, K. K., Babu, S. S. and Nair, V. S., (2011). 'The Optical and Physical Properties of Atmospheric Aerosols over the Indian Antarctic Stations during Southern Hemispheric Summer of the International Polar Year 2007–2008.' *Annales Geophysicae*, pp. 109–121. doi:10.5194/angeo-29-109-2011.

Chimot, J., (2017). 'Atmosphere Physical Structure.'

Crawford, J., Cohen, D. D., Stelcer, E. and Atanacio, A. J., (2017). 'Long Term Fine Aerosols at the Cape Grim Global Baseline Station: 1998 to 2016.' *Atmospheric Environment*, vol. 166, pp. 34–46. doi:10.1016/j.atmosenv.2017.07.012.

CSIRO, (2020a). 'Cape Grim Baseline Air Pollution Station.' https://research.csiro.au/acc/capabilities/cape-grim-baseline-air-pollution-station/.

CSIRO, (2020b). 'RV Investigator - MNF.' https://mnf.csiro.au/en/RV-Investigator.

Draxler, R. R. and Hess, G. D., (1998). 'An Overview of the HYSPLIT_4 Modelling System for Trajectories, Dispersion, and Deposition.' *Australian Meteorological Magazine*, vol. 47, p. 24.

Giles, D. M. and Holben, B. N., (2020). '2018 RV Investigator Cruise.' https://aeronet.gsfc.nasa.gov/new_web/cruises_new/Investigator_18_0.html.

Goody, R., (1995). *Principles of Atmospheric Physics and Chemistry*. Oxford University Press. ISBN 0-19-509362-3.

ian.umces.edu, (2020). 'IAN - Integration and Application Network, University of Maryland Center for Environmental Science.' https://ian.umces.edu/.

IPCC, (2013). *Climate Change 2013: The Physical Science Basis. Contribution of Working Group I to the Fifth Assessment Report of the Intergovernmental Panel on Climate Change*. Cambridge University Press, Cambridge, United Kingdom adn New York, NY, USA.

Josset, D., Pelon, J., Protat, A. and Flamant, C., (2008). 'New Approach to Determine Aerosol Optical Depth from Combined CALIPSO and CloudSat Ocean Surface Echoes.' *Geophysical Research Letters*, vol. 35(10). ISSN 1944-8007. doi:10.1029/2008GL033442.

Liu, B., Ma, Y., Gong, W. and Zhang, M., (2017). 'Observations of Aerosol Color Ratio and Depolarization Ratio over Wuhan.' *Atmospheric Pollution Research*, vol. 8, pp. 1113–1122. doi:10.1016/j.apr.2017.04.004.

Lumen, (2020). 'Global Atmospheric Circulations | Physical Geography.' https://courses.lumenlearning.com/geophysical/chapter/global-atmospheric-circulations/.

Mace, G. G. and Protat, A., (2018). 'Clouds over the Southern Ocean as Observed from the R/V Investigator during CAPRICORN. Part I: Cloud Occurrence and Phase Partitioning.' *Journal of Applied Meteorology and Climatology*, vol. 57(8), pp. 1783–1803. ISSN 1558-8424. doi:10.1175/JAMC-D-17-0194.1.

Merkulova, L., Freud, E., Mårtensson, E. M., Nilsson, E. D. and Glantz, P., (2018). 'Effect of Wind Speed on Moderate Resolution Imaging Spectroradiometer (MODIS) Aerosol Optical Depth over the North Pacific.' *Atmosphere*, vol. 9(60), pp. 1–19. doi:10.3390/atmos9020060.

Porter, J. N., Miller, M., Pietras, C. and Motell, C., (2010). 'Ship-Based Sun Photometer Measurements Using Microtops Sun Photometers.' *JOURNAL OF ATMOSPHERIC AND OCEANIC TECHNOLOGY*, vol. 18, p. 10.

R Core Team, (2019). 'R: A Language and Environment for Statistical Computing.' R Foundation for Statistical Computing.

RStudio Team, (2019). 'RStudio: Intergrated Development Environment for R.' RStudio Team, Inc.

Sikora, T. D. and Ufermann, S., (2004). 'Chapter 14. Marine Atmospheric Boundary Layer Cellular Convection and Longitudinal Roll Vortices.' In: 'Syntheitic Aperture Radar Marine User's Manual,' p. 10. U.S. Department of Commerce.

Smirnov, A., Holben, B. N., Sakerin, S. M., Kabanov, D. M., Slutsker, I., Chin, M., Diehl, T. L., Remer, L. A., Kahn, R., Ignatov, A., Liu, L., Mishchenko, M., Eck, T. F., Kucsera, T. L., Giles, D. and Kopelevich, O. V., (2006). 'Ship-Based Aerosol Optical Depth Measurements in the Atlantic Ocean: Comparison with Satellite Retrievals and GOCART Model.' *Geophysical Research Letters*, vol. 33(14). ISSN 1944-8007. doi:10.1029/2006GL026051.

Smirnov, A., Holben, B. N., Slutsker, I., Giles, D. M., McClain, C. R., Eck, T. F., Sakerin, S. M., Macke, A., Croot, P., Zibordi, G., Quinn, P. K., Sciare, J., Kinne, S., Harvey, M., Smyth, T. J., Piketh, S., Zielinski, T., Proshutinsky, A., Goes, J. I., Nelson, N. B., Larouche, P., Radionov, V. F., Goloub, P., Moorthy, K. K., Matarrese, R., Robertson, E. J. and Jourdin, F., (2009). 'Maritime Aerosol Network as a Component of Aerosol Robotic Network.' *Journal of Geophysical Research: Atmospheres*, vol. 114(D6). ISSN 2156-2202. doi:10.1029/2008JD011257.

Solar Light, (2020). 'MICROTOPS II Sunphotometer, Aerosol Optical Thickness Measurement.' https://solarlight.com/product/microtops-ii-sunphotometer/.

Tomasi, C., Vitale, V., Lupi, A., Carmine, C. D., Campanelli, M., Herber, A., Treffeisen, R., Stone, R. S., Andrews, E., Sharma, S., Radionov, V., von Hoyningen-Huene, W., Stebel, K., Hansen, G. H., Myhre, C. L., Wehrli, C., Aaltonen, V., Lihavainen, H., Virkkula, A., Hillamo, R., Ström, J., Toledano, C., Cachorro, V. E., Ortiz, P., de Frutos, A. M., Blindheim, S., Frioud, M., Gausa, M., Zielinski, T., Petelski, T. and Yamanouchi, T., (2007). 'Aerosols in Polar Regions: A Historical Overview Based on Optical Depth and in Situ Observations.' *Journal of Geophysical Research: Atmospheres*, vol. 112(D16). ISSN 2156-2202. doi:10.1029/2007JD008432.

Wallace, J. M. and Hobbs, P. V., (2006). *Atmospheric Science: An Introductory Survey*. Academic Press, Burlington, MA, 2nd edn. ISBN 0-12-732951-X.

Wandinger, U., (2005). 'Introduction to Lidar.' In: 'Lidar: Range-Resolved Optical Remote Sensing of the Atmosphere,' pp. 1–18. Springer Science+Business Media Inc., New York, NY, 1st edn. ISBN 0-387-40075-3.

Weller, R., Wöltjen, J., Piel, C., Resenberg, R., Wagenbach, D., König-Langlo, G. and Kriews, M., (2008). 'Seasonal Variability of Crustal and Marine Trace Elements in the Aerosol at Neumayer Station, Antarctica.' *Tellus B: Chemical and Physical Meteorology*, vol. 60(5), pp. 742–752. ISSN null. doi:10.1111/j.1600-0889.2008.00372.x.

A Appendix I

A.1 General Complexity R Coding

A.1.1 Plotting the raw and processed AOD Microtops sun photometer values

```
#The two datasets were merged by measurement date
    combinerawpro <- merge(raw,pro,by.x=2,by.y=1,all = TRUE)
    #The following line of code was used to limit the date and time on the graph
    lims <- as.POSIXct(strptime(c("2018-01-12 20:00", "2018-02-20 10:00"),format =
"%Y-%m-%d %H:%M"),tz="GMT")
    #The graph was produced with AOD on a logaritmic scale in order to clearly visualise
the data using the ggplot2 package.
    ggplot(comp,aes(date))+geom_point(aes(y=AOT500),shape=21,fill="lightgray",color="black",size=2)+
scale_y_log10()+scale_x_datetime(limits=lims)+labs(x="Date",y="Logarithmic scale of
Aerosol Optical Depth at 500 nm")+ annotation_logticks()+theme_minimal()
```

A.1.2 Plotting the processed AOD Microtops sun photometer values

```
#The code was the same as what was used for the combined raw and processed plot,
however only the processed dataset was used
    lims <- as.POSIXct(strptime(c("2018-01-12 20:00", "2018-02-20 10:00"),format =
"%Y-%m-%d %H:%M"),tz="GMT")
    ggplot(pro,aes(date))+geom_point(aes(y=AOD_500nm),shape=24,fill="orange",color="black",size=2)+
scale_y_log10()+scale_x_datetime(limits=lims)+labs(x="Date",y="Logarithmic scale of
Aerosol Optical Depth at 500 nm")+ annotation_logticks()+theme_minimal()
```

A.1.3 Plotting the violin plots

```
#The open source package was also used to create the violin plots.
    pro %>% ggplot(aes(x=month,y=AOD_500nm)) + geom_violin() + geom_boxplot(width=0.1)
+ ylim(0,0.2)
```